THE JOURNAL OF PHYSICAL CHEMISTRY B

Article

pubs.acs.org/JPCB

Structure and Dynamics of Extracellular Loops in Human Aquaporin-1 from Solid-State NMR and Molecular Dynamics

Shenlin Wang,[†,#,¶] Christopher Ing,[‡,§,¶] Sanaz Emami,[†,∥,¶] Yunjiang Jiang,[⊥] Hongjun Liang,[⊥] Régis Pomès,[‡,§] Leonid S. Brown,[*,†,∥] and Vladimir Ladizhansky[*,†,∥]

[†]Department of Physics, University of Guelph, Guelph, ON, Canada N1G 2W1

[‡]Molecular Structure and Function, Hospital for Sick Children, Toronto, ON, Canada M5G 1X8

[§]Department of Biochemistry, University of Toronto, Toronto, ON, Canada M5S 1A8

[∥]Biophysics Interdepartmental Group, University of Guelph, Guelph, ON, Canada N1G 2W1

[⊥]Department of Cell Physiology and Molecular Biophysics, School of Medicine, Texas Tech University Health Sciences Center, Lubbock, Texas 79430, United States

Supporting Information

ABSTRACT: Multiple moderate-resolution crystal structures of human aquaporin-1 have provided a foundation for understanding the molecular mechanism of selective water translocation in human cells. To gain insight into the interfacial structure and dynamics of human aquaporin-1 in a lipid environment, we performed nuclear magnetic resonance (NMR) spectroscopy and molecular dynamics simulations. Using magic angle spinning solid-state NMR, we report a near complete resonance assignment of the human aquaporin-1. Chemical shift analysis of the secondary structure identified pronounced deviations from crystallographic structures in extracellular loops A and C, including the *cis* Y37−P38 bond in loop A, as well as ordering and immobilization of loop C. Site-specific H/D exchange measurements identify a number of protected nitrogen-bearing side chains and backbone amide groups, involved in stabilizing the loops. A combination of molecular dynamics simulations with NMR-derived restraints and filtering based on solvent accessibility allowed for the determination of a structural model of extracellular loops largely consistent with NMR results. The simulations reveal loop stabilizing interactions that alter the extracellular surface of human AQP1, with possible implications for water transport regulation through the channel. Modulation of water permeation may occur as a result of rearrangement of side chains from loop C in the extracellular vestibule of hAQP1, affecting the aromatic arginine selectivity filter.

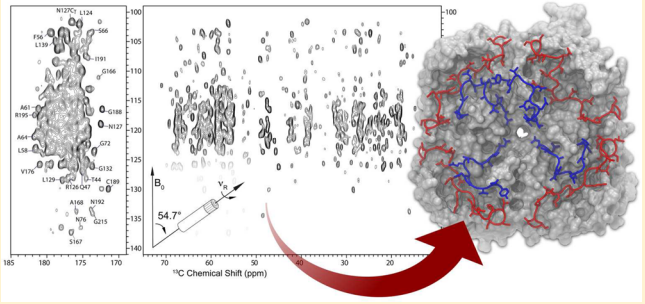

INTRODUCTION

Regulation of membrane water permeability is a fundamental requirement for all living organisms. Passive water transport across membranes is facilitated by aquaporins (AQPs), which have a wide taxonomic distribution and are found in vertebrates, invertebrates, plants, fungi, and bacteria. Humans have 13 different aquaporins (hAQP0−hAQP12), which are expressed in many vital organs and tissues. Their main function is to conduct water across cell membranes, although some AQPs are permeable to glycerol and other small solutes.[1,2]

Since their discovery, aquaporins have been a subject of active research, in part because of their medical relevance.[3,4] In particular, due to their possible involvement in a number of pathologies, aquaporins have been explored as pharmacological targets, and search for their inhibitors has been steadily expanding.[5−9]

Human aquaporin 1 is the first discovered human aquaporin, and it has been the focus of extensive structural studies by crystallographic methods: two medium-resolution cryo-EM structures and a medium-resolution X-ray crystal structure of hAQP1 are available,[10−12] as well as a higher-resolution structure of the homologous bovine AQP1.[13] In addition, there is a refined structural model of hAQP1 which is based on the EM structure of hAQP1 and the X-ray structure of its bacterial homologue GlpF.[14]

All structural data reveal a consensus tetrameric assembly of AQP1, with each monomer (28.5 kDa, 269 aa) acting as an independent bidirectional pore selectively permeable to water but rejecting other substances, such as ions (including protons) and other small molecules.[15−17] A topological model of hAQP1 is shown in Figure 1. Each subunit comprises six full α-helical transmembrane domains (H1−H6) and five loops connecting them (named A, B, C, D, and E). There are two additional short nonspanning helices inserted in the membrane, located in

Received: July 6, 2016
Revised: August 31, 2016

DOI: 10.1021/acs.jpcb.6b06731
J. Phys. Chem. B XXXX, XXX, XXX−XXX

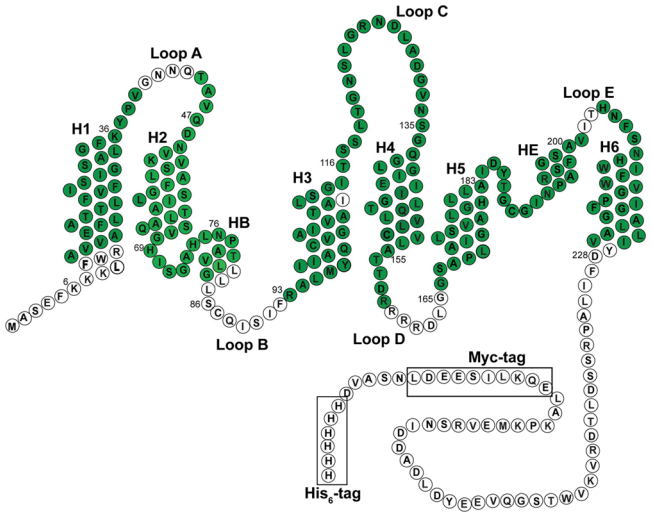

Figure 1. Topological model of hAQP1 with helices, loops, and purification His_6-tag and Myc-tag labeled. Residues shown in green have been assigned in the solid-state NMR spectra, as discussed in the Results section.

loops B and E (HB and HE). Helices HB and HE contain two characteristic NPA motifs (N76−P77−A78 and N192−P193−A194) at their ends. They fold into the bilayer from opposite sides of the membrane and form one of the constriction regions of the selectivity filter in the aqueous pore.[10,13,18] The other aromatic arginine constriction (ar/R) comprised of the highly conserved R195, H180, and F56 residues and C189 is responsible for physically excluding larger solutes. This so-called hourglass structure has high internal symmetry, whereby the protein can be viewed as two semichannels, which reflects the internal tandem sequence repeat.[19,20]

While the structure of transmembrane domains and the mechanism of water permeation are well understood on the basis of the available crystallographic, biochemical, and molecular dynamics simulations data, the conformations of less ordered and/or more mobile loops are not well-defined, and this is reflected in generally higher crystallographic temperature factors for these regions. At the same time, the biochemical data and MD simulations show that these regions may be important for regulation of water permeation, folding, oligomerization, and possibly other processes.[21−23] The extracellular entrance to the water conduction pore was also identified as a possible binding site for tetraethylammonium and other hAQP1-blocking compounds.[5,24]

Over the past two decades, solid-state NMR (SSNMR) has emerged as a powerful technique for studies of membrane protein structure and dynamics. SSNMR is not limited by the molecular weight of a protein, does not require long-range order, and can therefore be used to study membrane proteins in the bilayer environment under physiologically relevant conditions.[25−27] In this paper, we present a magic angle spinning (MAS) SSNMR study of hAQP1, and demonstrate that the important class of membrane-embedded water channels is amenable to structural analysis by MAS SSNMR. We report nearly complete resonance assignments obtained using multidimensional SSNMR of the protein reconstituted in lipids. Site-specific chemical shift and peak intensity analyses indicate no major differences in the secondary structure and mobility of the transmembrane (TM) domain between the NMR data and crystallographic structures but show large deviations for loop regions. Specifically, we detect the presence of a *cis* Y37−P38 peptide bond in loop A, as well as ordering and immobilization of loop C. Site-specific hydrogen−deuterium (H/D) exchange data of nitrogen-bearing side chains and backbone amide groups reveal a number of nonexchangeable atoms in loop C.

Using NMR-derived torsional restraints, molecular dynamics (MD) simulations, with multiple repeats resulting in microseconds of aggregate data, were used to generate an ensemble of structures representative of the NMR data. Our structural analysis suggests the existence of some stabilizing interactions of polar side chains in loop C with the TM domain of the protein and in some cases the extracellular loop A. While structures of several aquaporins do suggest stabilizing interactions in the extracellular region, our work provides strong evidence for such interactions based on the structural characterization of hAQP1 in a near-physiological state.

EXPERIMENTAL METHODS

Sample Preparation. The expression vector pPICZB-hAQP1-Myc-His6 (kindly provided by Frederick Öberg and Kristina Hedfalk, Göteborg University, Sweden)[28] encoding full-length hAQP1 with a C-terminal Myc and 6xHis tags was transformed into the protease-deficient *P. pastoris* strain SMD1168H (Invitrogen) by electroporation. Uniformly ^{15}N,^{13}C-labeled hAQP1 was expressed in *Pichia pastoris* using $(^{15}NH_4)_2SO_4$, $^{13}C_6$-labeled glucose, and ^{13}C-methanol as the sole nitrogen and carbon sources, respectively. HAQP1 was purified using Ni^{2+}-NTA resin and reconstituted into lipids (egg PC:brain PS = 9:1 w/w, Avanti lipids) by dialysis, at a protein/lipid weight ratio of 2, as described earlier.[29,30] Additional details are given in the Supporting Information.

NMR Spectroscopy. Proteoliposomes containing approximately 6 mg of UCN hAQP1 were center packed in a 3.2 mm thin wall rotor for NMR experiments. All SSNMR experiments were performed on a Bruker Avance III spectrometer operating at 800.230 MHz equipped with a 3.2 mm Efree HCN probe (Bruker USA, Billerica, MA). Measurements were performed at a spinning frequency of 14.3 kHz. The sample temperature was maintained at ∼5 °C in all experiments. Three-dimensional NCOCX, NCACX, and CANCO chemical shift correlation experiments were performed using previously described pulse sequences and optimization procedures.[31] For NCA and NCO transfer steps, band-selective SPECIFIC CP was implemented.[32] $^{13}C-^{13}C$ polarization transfers were implemented using DARR (dipolar assisted rotational resonance).[33,34] SPINAL-64 decoupling[35] of 86 kHz was used in both direct and indirect chemical shift evolutions. Carbon chemical shifts were indirectly referenced to 2,2-dimethyl-2-silapentane-5-sulfonic acid (DSS) by adjusting the position of the ^{13}C adamantane downfield peak to 40.48 ppm.[34] Nitrogen chemical shifts were referenced indirectly by using the ratio of gyromagnetic ratios γ_N/γ_C = 0.402979946. Additional details are given in the Supporting Information.

Molecular Modeling. Six tetrameric models of hAQP1 were constructed on the basis of the 3.8 Å electron microscopy structure (1FQY).[10] One model was left unmodified from the deposited EM structure. In five additional models (medoids A−E), the extracellular loops A and C were removed and reconstructed using MODELLER's "DOPE potential loop model"[36] with additional torsional potentials derived from TALOS+ predictions, identically for each subunit. During loop construction, a *cis* peptide bond was enforced between Y37 and

DOI: 10.1021/acs.jpcb.6b06731
J. Phys. Chem. B XXXX, XXX, XXX−XXX

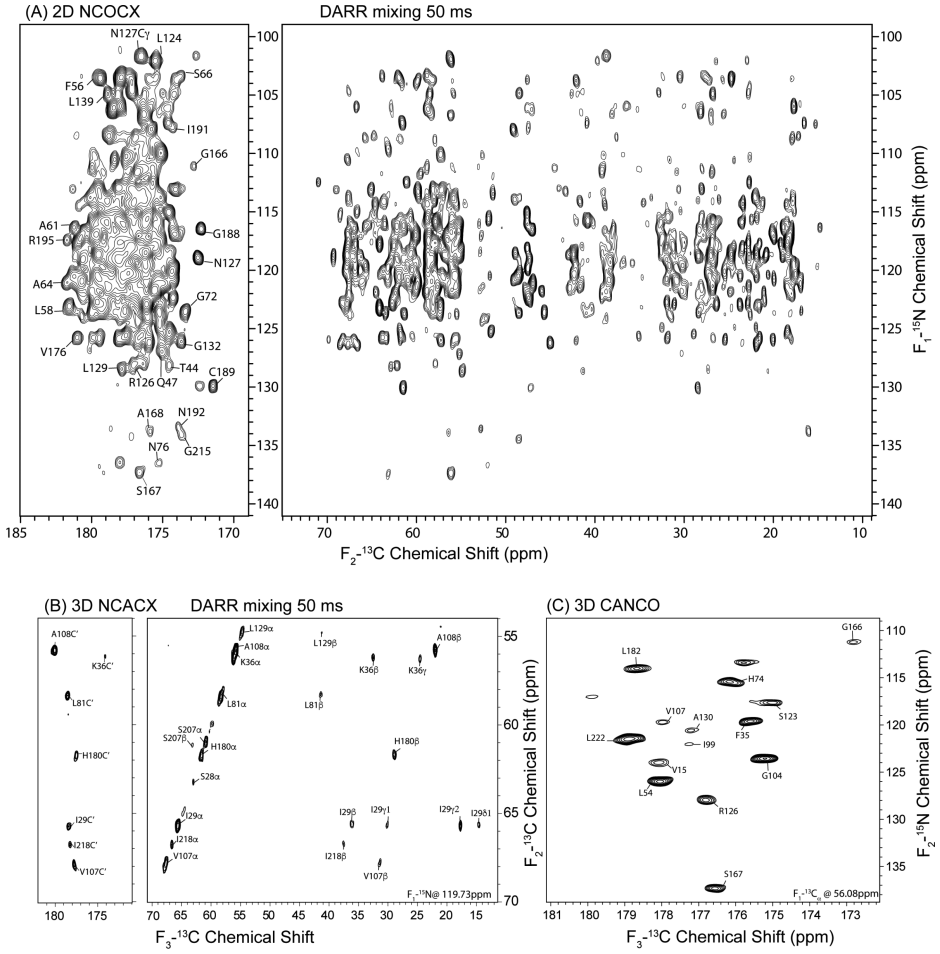

Figure 2. 2D and 3D SSNMR spectroscopy of hAQP1 at 800 MHz. (A) 2D NCOCX spectrum recorded with $^{13}C-^{13}C$ DARR mixing of 50 ms. Selected assignments shown in the NCO region of the spectrum are labeled according to the $C'[i]$ shift. (B) 2D plane of the 3D NCACX spectrum recorded with 50 ms DARR carbon−carbon mixing. Assignments are shown according to the $CX[i]$ shifts. (C) 2D plane of the 3D CANCO experiment. Assignments are labeled according to the $C'[i-1]$ shifts. In parts A and C, the first contour is taken at $5 \times \sigma$, with each additional level multiplied by 1.2. In part B, the first contour is cut at $4.5 \times \sigma$ with each additional level multiplied by 1.2.

P38 as predicted from NMR results (discussed below). Each tetramer was embedded in a solvated 1-palmitoyl-2-oleoyl-*sn*-glycero-3-phosphocholine (POPC) bilayer using g_membed[37] for a final simulation cell consisting of one hAQP1 tetramer, 272 POPC molecules, ~15,800 water molecules, 25 Na^+, and 33 Cl^- ions for a total of ~160,000 atoms. The protein, lipids, and ions were modeled with the CHARMM36 all-atom force field[38−40] along with the TIP3P[41] water model. The dimensions of the final simulation cell were $13.4 \times 14.1 \times 9.1$ nm^3.

MD Simulations. Simulations were performed using GROMACS 4.6.5.[42] For all six models, steepest-descent energy minimization was performed until atomic forces were less than 1000 kJ mol^{-1} nm^{-1}. Two replicas were spawned with different initial velocities for each of the six models, and were each simulated for 2 ns with protein heavy atom restraints with a force constant of 1000 kJ mol^{-1} nm^{-1}. Unrestrained production simulations of the 12 systems were carried out at constant temperature (300 K) and constant pressure (1 atm) for 500 ns each (6 μs in total). Restrained production simulations were carried out using the same initial condition and simulation methodology as unrestrained simulations, but torsional restraints derived from NMR chemical shifts were introduced on loop A and loop C of all subunits. The magnitudes of force constants utilized for restrained simulations are summarized in Table S2. Twelve simulations proceeded in four simulation blocks of increasing length and restraint (15, 50, 150, and 300−350 ns) for a total of 6 μs. Thus, the aggregate simulation time of the human AQP1 monomer was 48 μs across both unrestrained and restrained data sets. Additional details regarding molecular modeling and dynamics are described in the Supporting Information.

RESULTS

Sample Homogeneity and Solid-State NMR Spectral Resolution. Aquaporins are well-structured, predominantly helical proteins with a high propensity to form tetramers and assemble into functional two-dimensional square arrays in phospholipids.[43] We have previously reported a sample preparation protocol of fully functional hAQP1 reconstituted in lipids for MAS SSNMR and showed that most residues of the protein are visible in the dipolar correlation MAS SSNMR spectra and give rise to sharp lines with typical line widths on the order of 0.5 ppm in both ^{15}N or ^{13}C dimensions.[29] Small-angle X-ray scattering (SAXS) measurements indicate that hAQP1 forms a 2D tetragonal lattice in our samples, which gives rise to a series of scatterings at 0.096, 0.134, 0.192, 0.216, 0.272, 0.288, 0.346, 0.385, and 0.398 $Å^{-1}$, respectively, corresponding to the q_{10}, q_{11}, q_{20}, q_{21}, q_{22}, q_{30}, q_{32}, q_{40}, and

DOI: 10.1021/acs.jpcb.6b06731
J. Phys. Chem. B XXXX, XXX, XXX−XXX

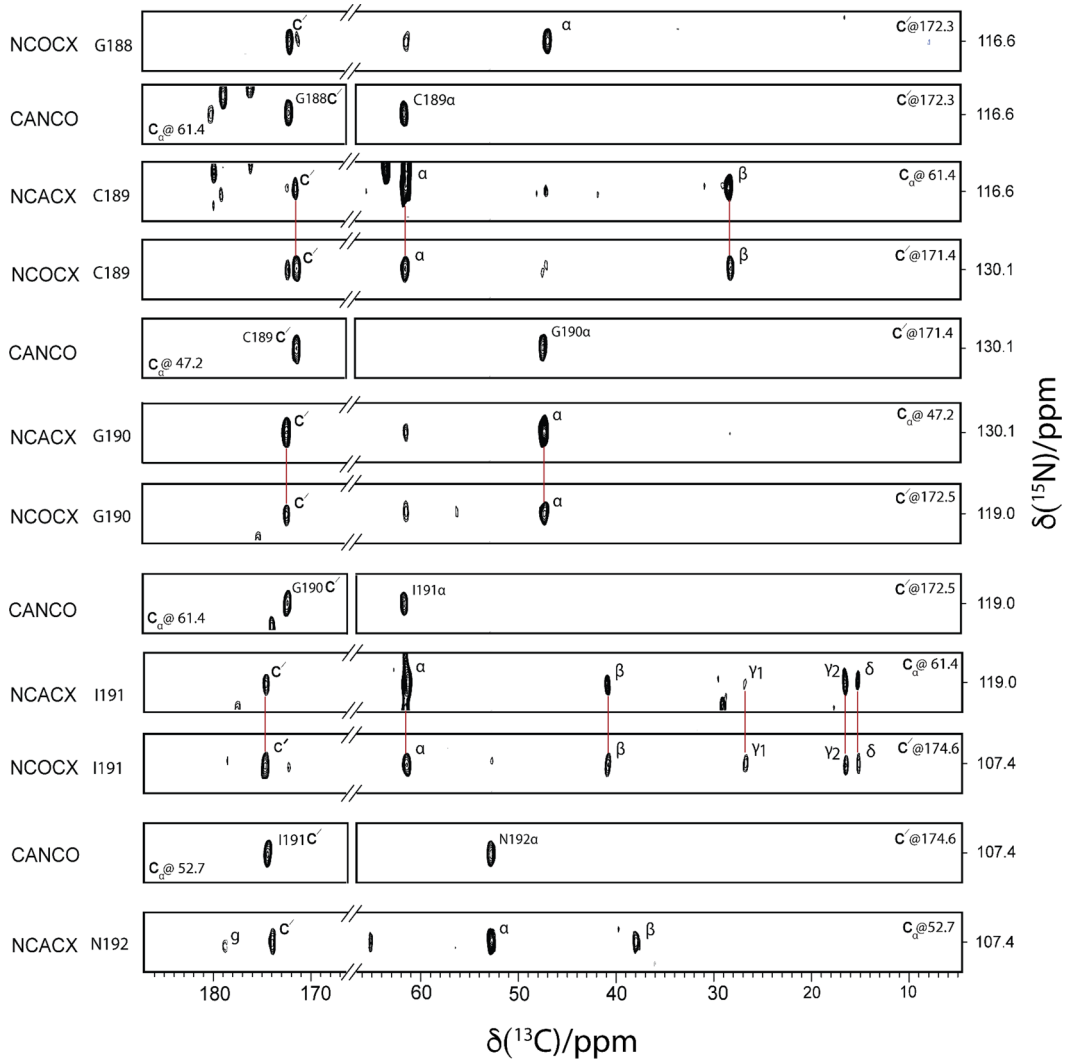

Figure 3. An example of a sequential assignment walk for residues G188−N192 in the ar/R constriction region of hAQP1. The lowest contour is cut at 5 × σ. NCOCX and NCACX strips are labeled by residue number according to the nitrogen shift, and Cα and C′ chemical shifts are given in each strip. Vertical lines link spin systems detected in the NCOCX and NCACX experiments. An additional example of the backbone walk is shown in Figure S2.

q_{41} peaks of a 2D hAQP1 square lattice with a lattice parameter of 65 Å (Figure S1, all scattering peaks marked by arrows). The first four peaks show up clearly, and the rest of the peaks at the higher q-range are weak but clearly discernible (Figure S1, inset). The AQP crystalline domain size estimated on the basis of the Scherrer equation[44] is ∼80 nm.

This 2D hAQP1 lattice agrees well with a previous TEM study,[43] which reported a 2D square lattice of hAQP1 with a lattice parameter of 96 Å. There was an oppositely oriented AQP tetramer resting in the center of each unit cell; i.e., two sets of oppositely oriented 2D hAQP1 square lattices were intercalated within each other. Given that the oppositely oriented hAQP1 tetramers are likely indistinguishable for X-ray scattering due to the similar electron density profiles of individual hAQP1 units,[19] SAXS is expected to observe a simple 2D square lattice with a lattice parameter $1/\sqrt{2}$ of that observed by TEM, i.e., ∼68 Å. However, we cannot rule out from SAXS data that all hAQP1 units in our sample are oriented in the same way, and they are closely packed to form a simple 2D square lattice.

This high degree of molecular 2D order goes hand in hand with the high atomic-level order, which is reflected in the high resolution of SSNMR spectra of hAQP1.

In Figure 2A, we show an example of a 2D NCOCX correlation spectrum, which contains many well-resolved cross peaks, even in the NCO region, which is generally heavily congested due to the limited dispersion of the carbonyl resonances. Still, there is considerable degeneracy and spectral crowdedness due to the large number of residues, and this degeneracy necessitates the use of 3D spectroscopy for spectroscopic assignments. An improvement of resolution in 3D spectra is demonstrated in Figure 2B and C, where we show 2D planes of the 3D NCACX and CANCO spectra, respectively.

Solid-State NMR Spectroscopic Assignments. For resonance assignments of hAQP1, we employed a combination of 2D and 3D homo- and heteronuclear correlation MAS NMR spectroscopies. The standard approach was described in detail elsewhere,[45−47] and is recapitulated in the Supporting Information. In Figures 3 and S2, we show two examples of a sequential backbone walk for residues G188−N192 and G125−

DOI: 10.1021/acs.jpcb.6b06731
J. Phys. Chem. B XXXX, XXX, XXX−XXX

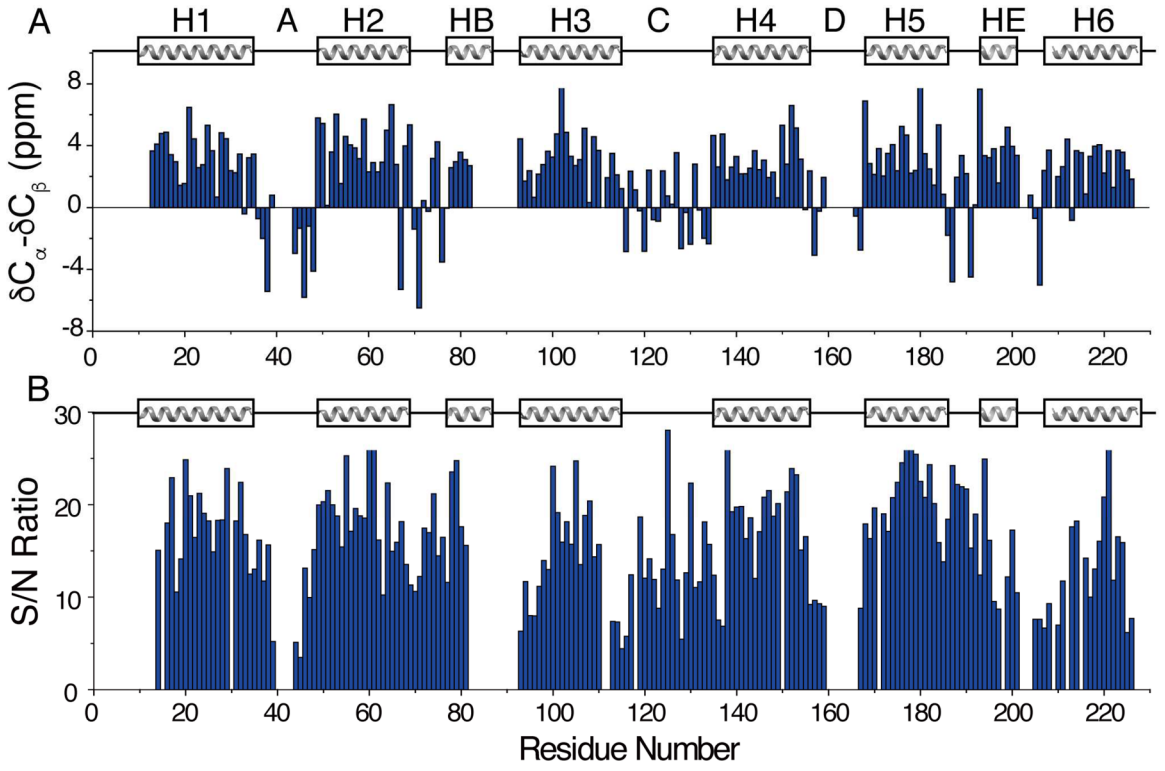

Figure 4. (A) Chemical shift index for human AQP1. Positive secondary shifts correspond to α-helical structure, while negative shifts indicate beta structure and other deviations from helicity. The secondary structure is shown on top to guide the eye, with designations of helices and loops according to the NMR data where available, and using crystallographic data for regions with incomplete assignments, e.g., helices H1 and HB. The two half-helices HB and HE are located in loops B and E. (B) Signal-to-noise ratios of cross-peaks detected in the 3D CANCO experiment shown as a function of residue number, according to the $C_\alpha[i]/N[i]$ assignments.

D131, respectively. The availability of nearly complete side chain resonances in the 3D NCACX, NCOCX, as well as 2D $^{13}C-^{13}C$ correlation experiments allows for an unambiguous identification of the amino acid type, and also permits matching of spin systems according to their side chain carbon shifts. Using these approaches, we have been able to obtain site-specific chemical shifts for a total of 192 out of 269 residues. Assignments have been deposited into the BMRB database under accession number 26805, and are summarized in Figure 1.

Secondary Structure Analysis. We have obtained nearly complete resonance assignments for transmembrane regions as well as for many residues in the loops. We infer the *cis* conformation of the Y37−P38 peptide bond from the large 10.8 ppm difference between the chemical shifts of P38 C_α and C_γ atoms.[48,49] We note that tyrosine, when preceding a proline, is known to stabilize the *cis* peptide bond conformation through aromatic−proline interactions.[50] The presence of the *cis* Y37−P38 bond is a new structural feature detected by SSNMR data, as no other structure of human or bovine AQP1 contains a *cis* Xaa−Pro bond at this position.

We further used C_α and C_β chemical shifts to analyze the backbone conformation of hAQP1 and compare it with the available crystallographic structures for both the human and homologous bovine AQP1. In Figure 4A, we show the chemical shift index (CSI)[51] constructed from C_α and C_β shifts as a function of residue number. There are six long stretches of positive secondary chemical shifts corresponding to membrane spanning helices H1−H6 and two shorter positive regions, corresponding to the non-spanning HB and HE half-helices found in loops B and E, respectively. There is generally a good agreement on the helical secondary structure of the TM regions between the NMR and the crystallographic data (Figure 1, Table S1). The agreement is especially good with the EM structure of lipid-embedded hAQP1 (PDB 1FQY).[10]

NMR chemical shifts reveal a number of distortions within α-helices. While most of them are located close to the protein−solvent interface (e.g., L33 in helix H1, K51 and V67 in helix H2), some occur in the middle of the TM regions. We observe a low CSI for A108 in helix H3 and at W213 in the middle of helix H6, with the latter distortion likely a kink caused by P216.

The largest discrepancies between the NMR data and crystallographic structures are observed for loop regions. We point to the fact that the crystallographic temperature factors are generally higher for loops, indicating their higher static disorder and/or higher degree of mobility. In contrast, single ^{13}C and ^{15}N chemical shift values and small line widths for all residues reflect conformational homogeneity of the protein.

Negative chemical shift indices in loop A suggest that this loop contains two short β-strands, comprising residues K36−P38 and T44−D48, which are unlikely to form a hairpin because of the distant relative position of helices H1 and H2. The first strand contains P38 in *cis* conformation, which may facilitate a bend (i.e., a region of high curvature[52]) in this loop.[53] These short strands are connected by a flexible linker, as evidenced by the reduced intensity of the NMR signals toward the ends of the two strands observed for V39, and T44 and A45, and by the absence of signals from residues in the G40−Q43 stretch in the spectra (Figure 4B).

DOI: 10.1021/acs.jpcb.6b06731
J. Phys. Chem. B XXXX, XXX, XXX−XXX

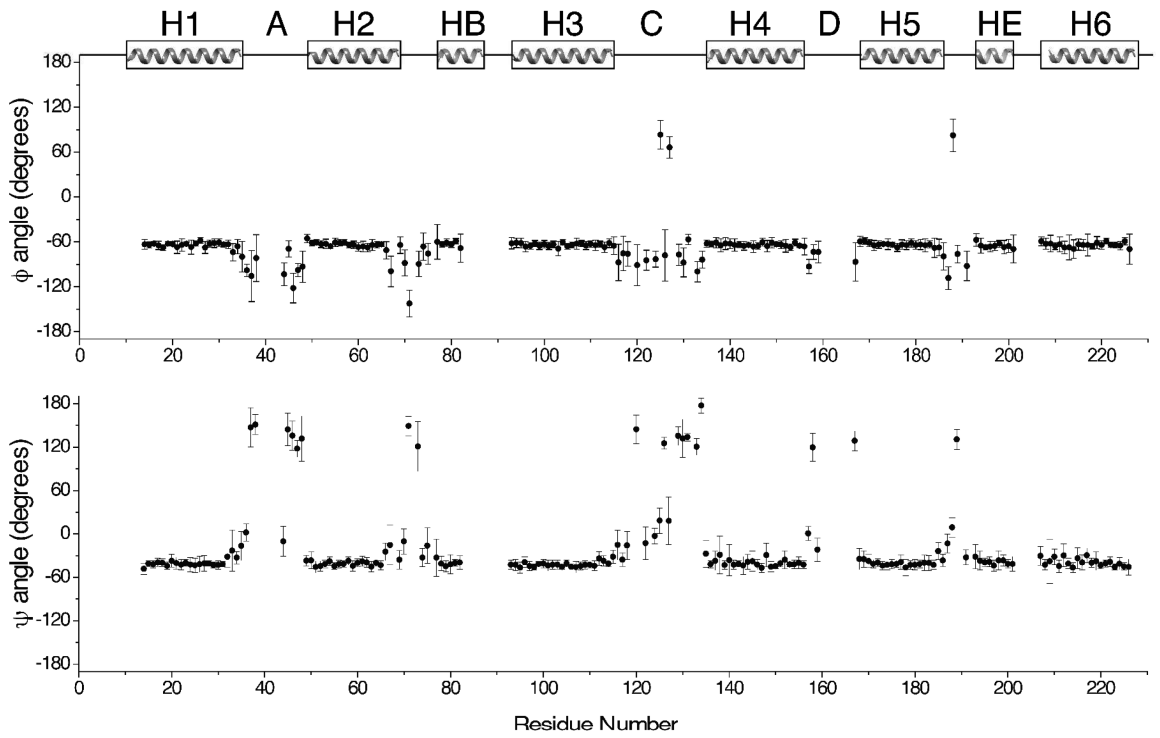

Figure 5. Backbone dihedral angles ψ, ϕ extracted from chemical shifts using the TALOS+ program.[54] Only values classified as "good" are shown. The secondary structure shown on top was derived from the NMR data and complemented with crystallographic 1FQY data for unassigned helical regions.

We observe a number of other interfacial regions where the signal is either attenuated or missing. In addition to the already mentioned reduction of intensity in loop A, no signal was detected for residues L83−F92 in loop B, including the end of half-helix HB and the part connecting HB and the following helix H3. Likewise, there was no signal detected for residues R160−G165 in loop D, whereas reduced intensities for the surrounding residues indicate an increased mobility of this loop as well. In contrast, the 19-residue-long loop C comprising residues T116−N134 appears to be less mobile, as the signal intensities for most residues in this loop are comparable to those in helices H3 and H4 (Figure 4B). Further examination of the site-specific CSI plot in Figure 4A indicates a potential ordered secondary structure in this loop, even though chemical shift index values tend to alternate between negative and positive values, and do not conform to a typical β-strand or α-helical CSI patterns.

To gain additional insight into hAQP1 secondary structure, we extracted backbone torsion angles using the TALOS+ program.[54] The extracted angles for TM regions, shown in Figure 5, are in close agreement with the dihedral angles derived from crystallographic data, and indicate well-ordered transmembrane helices with no obvious deviations from helicity. Minor deviations indicated by the CSI analysis and discussed above are too small and cannot be resolved by TALOS+.

The conformations of both loops A and C are different from those suggested by the crystallographic data. The TALOS+ predictions for loop A are consistent with β-structure and further corroborate the existence of a short beta strand for residues T44−D48. TALOS+ angles for loop C indicate β-sheet structure for residues L129−N134 with torsion angles (ϕ, ψ) varying between −56 and −100° and 120 and 177°. Near the middle of loop C, TALOS+ also predicts that a β-turn is formed by R126−N127 with their (ϕ_{i+1}, ψ_{i+1}), (ϕ_{i+2}, ψ_{i+2}) angles being close to (−60°, 120°), (80°, 0°) of an ideal type II β-turn.[55] These predictions will be further validated through the use of restrained molecular dynamics as described below.

Hydrogen−Deuterium Exchange and Water Accessibility. To obtain additional information on the nature of the interactions stabilizing loop conformations, we carried out NMR hydrogen/deuterium (H/D) exchange experiments. In an H/D experiment, we compare backbone signal intensities detected in 2D NCA and 3D NCACX experiments, and side chain signal intensities (we could observe several Arg, Gln, Asn, and His residues) obtained from the same protein sample first prepared in a H_2O-based buffer and then incubated for 24 h in a D_2O-based buffer.[47,56,57] Because the NMR signal is generated from the amide or side chain protons in these experiments, residues with protons that exchange with D_2O yield a reduced signal, while signals from inaccessible residues or residues protected by hydrogen bonds are less attenuated. In Figure S3, we show representative $^{15}N/^{13}C$ planes of the 3D NCACX experiment collected in H_2O and D_2O buffers, where the effect of the H/D exchange is readily visible.

A site-specific comparison of the NMR backbone signals detected in H_2O and D_2O is shown in Figure 6A. We observed an overall reduction of signal for the entire protein, which may indicate partial low-level exchange and/or sample losses during incubation in D_2O and subsequent removal of the excess buffer. The amide protons of residues located in TM helices are protected and do not exchange except in the flanks of some of the helices.

In contrast, the exposed loops A, C, and D are mostly exchangeable with some notable exceptions in loop C, where A130, V133, and N134 within the ordered part of that loop are likely protected by strong hydrogen bonding, either within the loop or with some of the side chains. Interestingly, the

DOI: 10.1021/acs.jpcb.6b06731
J. Phys. Chem. B XXXX, XXX, XXX−XXX

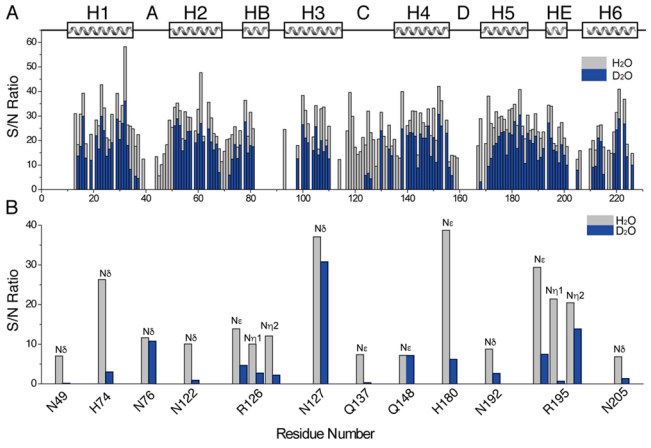

Figure 6. (A) Comparison between backbone amide cross peak intensities from hAQP1 incubated in H_2O (gray) and D_2O (blue) based buffers. (B) Comparison of cross peak intensities corresponding to nitrogen-bearing side chain signals detected in the H/D exchange experiments. Gray bars represent intensities in H_2O; blue bars are intensities detected after 24 h of incubation in D_2O.

homologous loop of bovine AQP1 shares the AxxVN motif and its X-ray structure shows hydrogen bonding of backbone amide nitrogen atoms of the alanine and valine to carbonyl oxygen atoms of the respective $i - 2$ residues.[13]

The exchangeability of nitrogen-bearing side chains shown in Figure 6B provides additional information on their solvent accessibility and hydrogen bonding, some of which could not be deduced from the available structures of hAQP1. While some of the solvent-exposed side chains found on the cytoplasmic (H74) and extracellular (N49, N122, R126, Q137, H180, N205) ends of the protein are exchangeable as expected, several residues are fully or partially protected from the H/D exchange. Whereas Q148 is buried facing the middle of the bilayer in all structures and is nonexchangeable, several other residues located either on the extracellular surface or in the water-filled pore are expected to be solvent-accessible but found to be nonexchangeable or partially exchangeable in the NMR data. In particular, the two asparagines of the NPA motifs in the pore are either not exchangeable (N76) or only exchangeable on a very slow time scale (weeks, N192). This is surprising, considering that they are in contact with water molecules in the X-ray structure of bAQP1.[13] Similarly surprising is the lack of exchange of N127 of loop C and the partial exchange of R195 of the ar/R filter, which suggest their involvement in strong H-bonding.

Additional information on hydrogen bonding of some side chains can be inferred from their chemical shifts. In particular, the chemical shifts of terminal carbons of carboxylic side chains (Asp and Glu) correlate with their protonation state and hydrogen bonding: protonated and buried deprotonated carboxylic acids have lower chemical shifts than exposed deprotonated ones.[58,59] HAQP1 has two glutamates, E17 and E142, symmetrically located in the intracellular and extracellular channel vestibules, each interacting with the backbone of their adjacent half-helices, HB and HE, respectively.[60] Interestingly, E142 C_ε has a much lower chemical shift than E17 (179.5 vs 182.6 ppm), suggesting much stronger hydrogen bonding of E142, which may also correlate with the anomalously high chemical shift of the amide nitrogen of G190 (116.6 ppm), to which E142 is hydrogen-bonded in the bAQP1 structure.[13] Similarly, assigned aspartic acids show chemical shifts of C_γ carbons ranging from those typical for exposed carboxyls for D48, D158, and D185 (loops A, D, and E, respectively) to buried hydrogen-bonded ones for D128 (loop C). The latter may be involved in stabilizing interactions of loop C.

Summary of Experimental Findings. The analysis of NMR data suggests that loops A and C retain partial structure. Loop A consists of two short beta strands, which are unlikely to interact with each other to form a beta-hairpin. The first strand contains *cis* P38 which is not found in any of the published structures of human and bovine AQP1. Although single chemical shift values for residues in these strands suggest their single conformations, one cannot rule out fast motions of small amplitudes within the strands. A flexible linker connects the strands, and its reduced and missing NMR intensities suggest that it is highly dynamic.

In contrast, on the basis of its cross peak intensities, loop C appears to be largely immobilized, and H/D exchange patterns suggest a few stabilizing interactions: nonexchangeable backbone amides of residues 130, 133, and 134 as well as the lack of H/D exchange for side chain nitrogen atoms of N127 and the low chemical shift of the terminal carbon of D128 are all indicative of strong H-bonding.

What are the interactions stabilizing the preferred conformations of loops A and C? Although some of this information can be inferred from the available structures, the discrepancies between the NMR and crystallographic data, the high B-factors for the loop regions, and the presence of several nonconservative replacements in loop C between the bovine and human variants of AQP1 (e.g., D121G, L126R, A128D, and P131D using human numbering) warrant further investigation. We used molecular dynamics simulations to assist in the interpretation of the NMR results, and to obtain an ensemble of preferred loop A and loop C conformations that are in agreement with both the predicted torsion angles and the observed H/D exchange patterns.

Computational Modeling and Simulation Approach. We chose the tetrameric electron microscopy model of hAQP1 (1FQY)[10] as our initial molecular model because it agrees best with the helical boundaries determined from NMR chemical shifts (Table S1). Our experiments suggest that the conformations of loops in the EM model of hAQP1 may be non-native,[10] making their study with conventional molecular dynamics simulations computationally challenging. For that reason, we used the following approach to generate an ensemble of loop conformations consistent with NMR data: we constructed six models of hAQP1 with varying initial loop A and C conformations, we imposed TALOS+ derived restraints during both homology modeling and molecular dynamics, and we performed multiple simulation repeats of the hAQP1 tetramer.

One initial model for MD simulations was built with the original conformation of loops A and C (referred to as "Crystal Structure" or "XTAL"), and five additional models, referred to as medoids A–E, were constructed using the crystal structure as a homology modeling template but with *de novo* modeling of loops A and C. Our homology modeling protocol included TALOS+-derived restraints and a *cis* Y37–P38 bond, in addition to the MODELLER loop modeling potential energy function.[36] We clustered the best-scoring models from homology modeling and extracted cluster medoids to obtain distinct initial conditions for our simulations (Methods, Figure S4A).

DOI: 10.1021/acs.jpcb.6b06731
J. Phys. Chem. B XXXX, XXX, XXX–XXX

All-atom MD simulations were performed on all six hAQP1 models in a hydrated lipid bilayer. Root-mean-square deviation (RMSD) calculations indicate that none of the six initial loop conformations persisted after the initial equilibration procedure. Within the residues forming loops A and C together with two additional residues flanking each of these loops, TALOS+ predictions for all assigned residues classified as "Good" were included as torsional restraints in the restrained MD simulations (Table S2). Five residues in the middle of loop A (V39−Q43) and five residues in loop C (L119, G121, S123, D128, and G132) could not be assigned or were assigned a "Warning" by TALOS+ and therefore were not assigned torsional angle restraints in simulations. The magnitude of torsional restraint force constants was successively increased over four simulation periods, but even in their strongest form, they were relatively weak (5−50 kJ/mol/rad^2) in order to minimally perturb the energy landscape of the protein. Unrestrained simulations of equal length were completed as a control to assess the effect of the restraints on loop structure and dynamics (Figure S4B). In both unrestrained and restrained MD simulations of all models, two simulation repeats with randomized initial atomic velocities were performed in order to improve statistical sampling. Using two simulation repeats of the full hAQP1 tetramer increased sampling of loop A and C conformations 8-fold. Additional details regarding model construction and simulation protocols are presented in the Methods and Supporting Information.

Effect of TALOS+-Derived Restraints on MD Ensembles. The effect of backbone torsional restraints on loops A and C was evaluated by computing the deviation from TALOS + predicted angles using several approaches. In control simulations without restraints, the average angular RMSD from TALOS+ predictions in the loops approached a stable value after 150−200 ns of simulation but did not tend toward TALOS+ targets over the full length of simulation time (Figure S5A−C). Torsional restraints reduced the angular RMSD of loop A and loop C from TALOS+ predictions by more than half, approaching an average of 15−30° for all models (Figure S5D−F). Despite this apparent convergence of average backbone torsions, extracellular loops were found to sample a heterogeneous distribution of φ and ψ angles across all models (Figure S6). The coincident agreement of all φ and ψ angles to TALOS+ targets of loop C was significantly higher in the restrained simulations than in the unrestrained simulations (Figure S7B).

Although the use of multiple homology models, TALOS+ derived restraints, and multiple simulation repeats assists in obtaining structures consistent with NMR, it is not expected that loop A and C conformations will necessarily relax to a global energy minimum on the time scale of our simulations (hundreds of nanoseconds).[61] This limitation is due in part to the experimental design of our simulations, in which only weak torsional restraints were applied to a subset of all loop A and C residues. As such, we used additional criteria to extract conformations from this ensemble that are in agreement with experimentally determined backbone torsions and H/D exchange data.

The effect of loop A and C conformations on the function of AQP1 was investigated by computing mean water permeability (p_f) from unrestrained and restrained simulations (Figure 7). This quantity (presented in units of 10^{-14} cm^3/s) was computed separately for each monomer of each simulation repeat using the theoretical framework proposed by Zhu et al.[62]

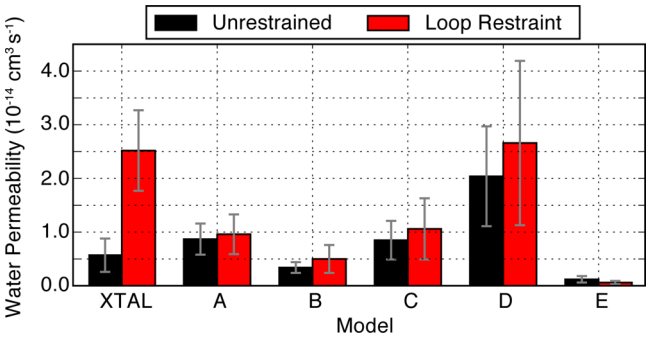

Figure 7. Water permeability computed from MD simulations. Mean permeability is computed using all subunits of both simulation repeats for each model (XTAL, Medoid A−E). Data is shown for unrestrained (black) and loop restrained (red) data sets.

In unrestrained simulations, the mean p_f was 0.57 ± 0.31, 0.87 ± 0.29, 0.34 ± 0.10, 0.85 ± 0.36, 2.04 ± 0.93, and 0.12 ± 0.06 for XTAL and medoid A−E simulations, respectively. In restrained simulations, the mean p_f was 2.52 ± 0.75, 0.96 ± 0.37, 0.50 ± 0.26, 1.06 ± 0.57, 2.66 ± 1.53, and 0.06 ± 0.03 for XTAL and medoid A−E simulations, respectively. With the exception of XTAL (highest p_f) and medoid E (lowest p_f), water permeabilities were identical within error across all models. Upon introducing loop restraints, water permeability increased by a factor of 4 for the XTAL model, but the remaining models did not change beyond the error of our calculations.

Analysis of Loop Conformations. Secondary structure analysis was performed on loops A and C in order to compare MD simulation results with TALOS+ predictions. Loop A was found to be predominantly in the "coil" conformation with transient populations of both "helix" and "extended" conformations [less than 20% of frames for most residues, using a secondary structure analysis algorithm[52] (Figure 8A)]. Across all models, a hydrogen-bonded turn in loop A varied in position from G40 to T44, indicating a significant structural diversity within our ensemble. In 10% of frames of three models, a short α-helical turn was adopted in a stretch of residues (V39−T44) where torsional restraints were applied only to one residue (T44) (Figure 8B, I). This α-helical turn was not stabilized by any inter- or intramonomer interactions. In 5% of frames of medoid A, short parallel β-strands were formed between residues A45−V46 and V46−Q47 of adjacent subunits (Figure 8B, II). Although this state was not highly populated, it is within the TALOS+ deviation expected for our restraints (wherein adjacent subunits had an average backbone torsional deviation from TALOS+ predictions of {17 and 14°} and {19 and 23°}, for ψ and ϕ angles, respectively). Predominantly in medoid E, the signature hydrogen-bonded turn in loop A was also stabilized by a V39 to N42 backbone interaction (Figure 8B, IV). In simulations of the crystal structure and of medoids A and E, there was a significant propensity for residues G121 to 125 in loop C to form a helical turn, a state with an average TALOS+ deviation of 9 and 21° for restrained ψ and ϕ angles in that region, respectively (Figure 8B, III and V).

A structural feature of loop C with high propensity in all models is a hydrogen-bonded turn between residues A130 and V133 (residues i to i + 3). In close proximity, medoid E had a high population of parallel β-bridge (defined as two consecutive hydrogen bonds which are characteristic of beta structure[52]) between L129 and G188 (Figure 8B, VI). Although this β-

DOI: 10.1021/acs.jpcb.6b06731
J. Phys. Chem. B XXXX, XXX, XXX−XXX

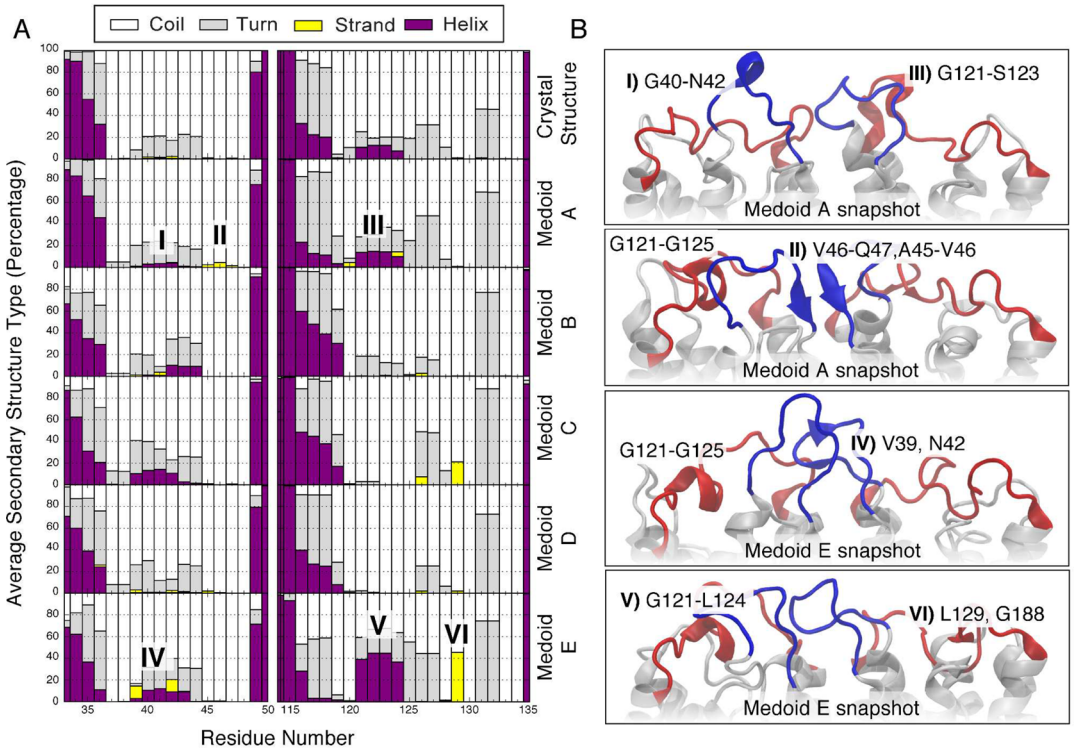

Figure 8. Average secondary structure propensity of loop A (blue) and loop C (red) residues in MD simulations. (A) Secondary structure propensities (coil in white, turn in grey, strand in yellow, helix in purple) from restrained simulations averaged over all simulation frames of monomers and repeats of each model. Secondary structure elements labeled with Roman numerals correspond to molecular renderings. (B) Molecular renderings of two adjacent hAQP1 monomers exhibiting intra- and interdomain secondary structure. Labels indicate segments of residues involved in secondary structure formation.

bridge is not formed in all models, similar backbone interactions in this region were found in other models (Figure 8B, V and VI) that appear to stabilize the hydrogen-bonded turn at D131 and G132.

In order to study common structures of loop C and compare them to solvent accessibility data, all conformations from the five medoids were pooled and clustered. Eight clusters were generated using pairwise RMSD between all simulation frames as a metric, with cluster populations of 16, 14, 10, 13, 12, 12, 18, and 5%, respectively. The similarity of the eight cluster centers was quantified with a pairwise loop C RMSD matrix (Figure 9A). As expected by our use of multiple initial models with sparse torsional restraints, each cluster contained diverse loop C conformations (Figure S8).

To identify conformations in qualitative agreement with the H/D exchange data, we computed the backbone and side chain nitrogen solvent accessibility for each of the clusters in the restrained data set (Figure S9). Across all residues, there is a general agreement with backbone nitrogen H/D exchange where data are available (Figure 6), but site-specific discrepancies exist between clusters. Clusters 1–4, 7, and 8, which make up 76% of the conformationally restrained data set, contain protected backbone nitrogen atoms of residues A130, V133, and N134 in good agreement with the H/D exchange data (Figure 6A), forming a hydrogen-bonded turn (Figure S9A). Molecular renderings of these residues in buried states (cluster 7) as well as solvent-exposed states (cluster 6) are depicted with corresponding hydrogen-bonding residue profiles of loop C (Figure 9B). This analysis suggests that, despite the use of weak torsional restraints on disparate models, there are common structural motifs observed in the backbone of loop C. However, the clusters in qualitative agreement with backbone solvent accessibility were not found to be in as good an agreement with the experimental H/D exchange pattern of side chain nitrogen atoms (Figure S9B). Whereas side chain nitrogen atoms of H74, N122, R126, and H180 were all found to be solvent-exposed in simulation (Figure S9B) in agreement with the exchange data (Figure 6), the side chain of N127 was solvent exposed in the majority of frames as well in all clusters (Figure 9C). Despite this qualitative disagreement, we extracted several configurations of loop C in which the N127 side chain was forming protein hydrogen bonds (N127 interactions with S196, N205, and T203) (Figure 9C). In all clusters, we examined the burial of the aspartic acid D48, D128, and D185. D48 is peripheral to loop A and adjacent to N49, the side chain of which was suggested to form a stabilizing interaction with D185 on a neighboring α-helix.[21] The carboxylate groups of D48 and D185 were both involved in protein hydrogen bonds in ~9–10% of frames, suggesting that they are still predominately solvent-exposed. In the case of D185, these protein–protein hydrogen bonds involved exclusively N49. The C_γ chemical shift of D128 suggests that this side chain may form strong hydrogen bonds. In the simulations, one or both of the D128 carboxylate oxygen atoms were found to form protein–protein hydrogen bonds in 15, 11, 39, 27, 27, 14, 17, and 11% of frames in each of the eight clusters, respectively. The hydrogen-bonding partners of D128 include the side chains of K36, N42, and R195. The high propensity for solvent exposure of N127 and D128 in the simulations is likely due to the slow relaxation of side chains from the initial out-of-equilibrium conformations. To reduce this effect, we further filtered the restrained data set using two

DOI: 10.1021/acs.jpcb.6b06731
J. Phys. Chem. B XXXX, XXX, XXX–XXX

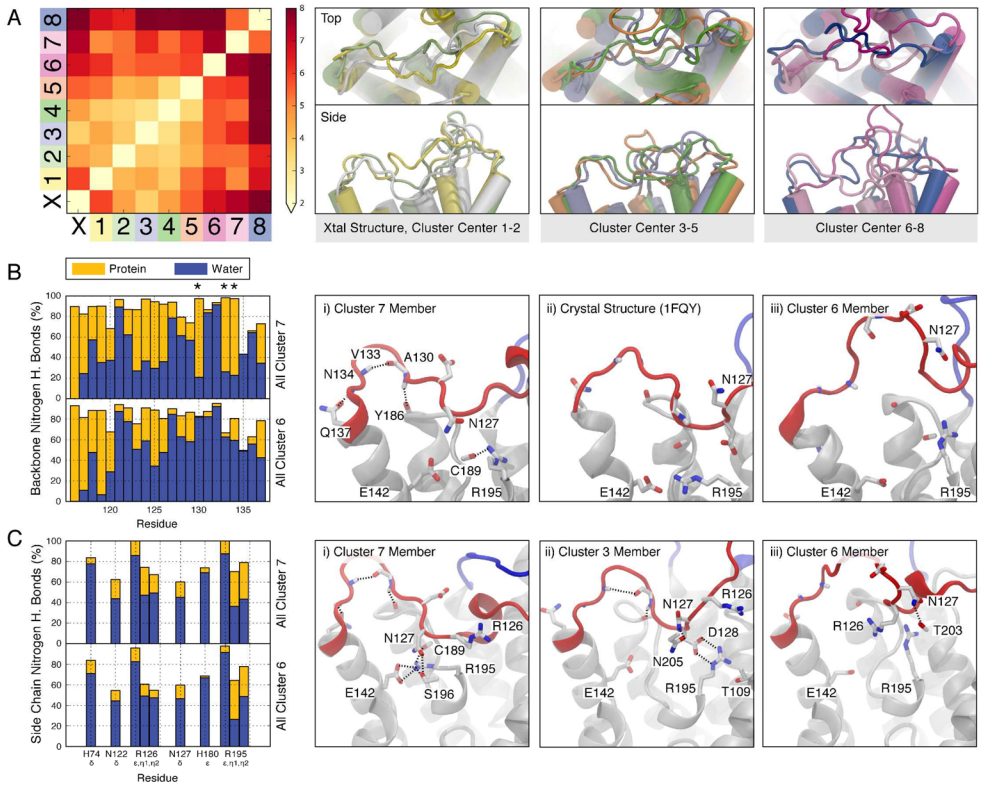

Figure 9. RMSD-based clustering of loop C across MD simulations of all homology models. (A) Pairwise loop C RMSD matrix of the crystal structure (1FQY) and eight structures representative of cluster centers from clustering of restrained simulations (left) along with molecular renderings of loop C cluster centers where residue 185−192 and 185−214 are hidden in the top and side orientations, respectively (right). The RMSD matrix color bar is in units of Å. (B) Probability of loop C backbone nitrogen atoms hydrogen-bonding to protein or water molecules from restrained simulations. Results from two clusters are depicted that have low and high qualitative agreement to H/D-exchange experiments, clusters 6 and 7, respectively (left). Representative frames are depicted from these clusters with key residues identified from H/D-exchange experiments (A130, V133, and N134; right). (C) Probability of loop C side chain nitrogen atoms hydrogen-bonding to protein or water molecules from restrained simulations. Results from two clusters are depicted that have low and high qualitative agreement to H/D-exchange experiments, clusters 6 and 7, respectively (left). Representative frames from these clusters depict transient N127 side chain burial in agreement with H/D-exchange experiments (right).

different metrics: the conformational state of R195 and the agreement of our data to experimental solvent-accessibility profiles of multiple nitrogen atoms, allowing us to examine hydrogen-bonding patterns in a subset of data in highest agreement with experimental results.

H/D exchange experiments indicate exchangeability for only one of the terminal nitrogen atoms of R195 (Figure 6B). This finding motivated a detailed analysis of the hydrogen-bonding environment around R195 and the involvement of this residue in stabilizing loop C. In the simulations, the R195 side chain adopted either a down-facing state (toward E142), similar to the 1FQY EM structure of hAQP1,[10] or an up-facing state (toward loop C), in which R195 was frequently hydrogen-bonded to N127 or D128, resembling the 1IH5 or 4CSK structures of hAQP1.[12,13] In both conformations, the R195 side chain sampled orientations in which one of two terminal nitrogen atoms was buried from solvent. However, on average, the difference in protein−protein and protein−water hydrogen bonds formed with either of the terminal nitrogen atoms was less than 20%, suggesting minimal asymmetry across the entire conformationally restrained data set (Figures 9C and S9B). Computing the solvent accessibility of loop C separately for two distinct side chain conformations of R195 characterized by mutually exclusive hydrogen bonding to E142 or N127/D128 shows that neither state agrees with the predictions from H/D exchange (Figure S10). The up-facing and side-facing states of R195 had 63 and 53% of frames satisfying the experimental backbone hydration of A130, V133, and N134, respectively, suggesting that the up-facing state may be more conducive to the stabilization of loop C. However, the predicted side chain nitrogen burial of loop C remained low, suggesting that the orientation of R195 is not the sole determinant of the loop conformations characterized experimentally.

Although clustering loop conformations and partitioning the ensemble according to distinct rotameric states of R195 helped to characterize the structural properties of the conformationally restrained data set, this analysis was not sufficient to extract loop conformations consistent with all available NMR data simultaneously. To extract a subset of conformations in agreement with both backbone and side chain nitrogen solvent accessibility, we analyzed the protein−protein hydrogen bonds of key residues as a means to compare qualitatively to H/D exchange accessibility profiles. In this analysis, we assume that protons engaged in protein−protein hydrogen bonds are not exchangeable and, conversely, that exchangeable protons do not make protein−protein hydrogen bonds. This criterion may miss conformations in which a nitrogen group should have been classified as buried on the basis of its surrounding environment but does not meet our hydrogen bonding criteria (as defined in the Supporting Information). An upper bound

DOI: 10.1021/acs.jpcb.6b06731
J. Phys. Chem. B XXXX, XXX, XXX−XXX

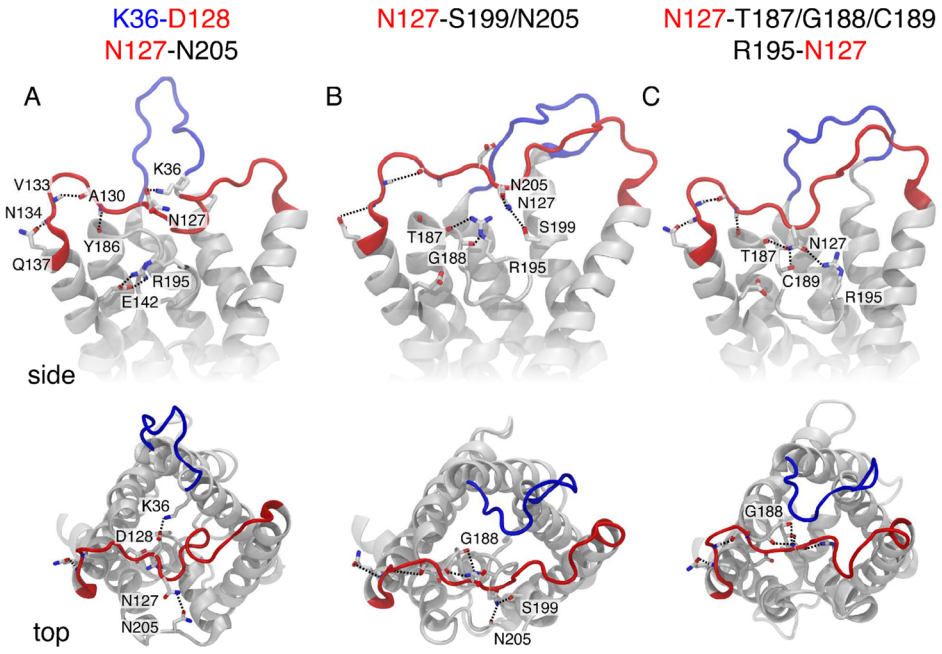

Figure 10. Representative snapshots of hAQP1 from TALOS+ restrained simulations where site-specific solvent accessibility was in agreement with H/D-exchange experiments and key loop A (blue) and C (red) hydrogen bonds were formed. The extracellular region of hAQP1 is shown from side and top orientations, where the side view omits residues 196−215 for clarity. Structures were manually selected on the basis of the results of a hydrogen-bonding analysis of loop A and C residues. A dashed line (black) indicates the presence of a hydrogen bond. Water is omitted for clarity. In these snapshots, the backbone nitrogen atoms of A130, V133, and N134 and the side chain nitrogen atom of N127 are involved in protein−protein interactions.

on the number of potentially misassigned frames (in which NH groups are not involved in either protein−protein or protein−water hydrogen bonds) is shown in Figure S9B for key nitrogen groups. Hydrogen bonds between lipid head groups and loop C residues are not depicted in Figures 9 and S9. Consistent with a previous study of protein−lipid interactions in aquaporin,[63] we observed interactions of I115−S117 and S135−Q137 with lipid head groups in restrained simulations. Additionally, either of the two terminal nitrogen atoms of R126 formed a lipid hydrogen bond in an average of 22 ± 8, 33 ± 14, 21 ± 10, 0 ± 0, 6 ± 5, and 21 ± 8% simulation frames for XTAL and medoids A−E, respectively. Although R126 is predicted to be solvent exposed in H/D exchange experiments, lipid interactions may nonetheless contribute to the stabilization of loop C.

Out of the 76% of frames in which backbone nitrogen solvent accessibility is largely satisfied (clusters 1−4, 6, and 7), 3% are consistent with side chain solvent accessibility profiles. Here we examine protein−protein hydrogen bonds involving loops A and C within this smaller subensemble and render several snapshots broadly consistent with NMR experiments (Figure 10). In approximately 37% of these conformations, the side chain nitrogen of residue K36 (loop A) forms a salt bridge with the carboxylate group of D128 of loop C, providing a possible stabilization mechanism (Figure 10A). This result is in contrast to the 1FQY EM structure[10] in which D128 adopted a down-facing state toward R195. Note that simulations suggest that the orientation of R195 may only moderately affect the conformation of loop C (Figure S10). An alternative interaction stabilizing loop C suggested by MD is a hydrogen bond between the backbone groups of D128 and G188, found in 33% of frames. The neighboring residue of K36 in loop A, Y37, also forms hydrogen bonds between its side chain hydroxyl and backbone oxygen atoms of G121 and S123 in 6 and 4% of conformations, respectively. P38 does not make significant hydrogen bonds outside of loop A, although V39 backbone nitrogen atoms formed contacts with T120 in 15% of conformations. Within the same subensemble of 3% of the restrained data set, the side chain nitrogen atom of N127 was hydrogen bonded to T187, G188, or C189 backbone oxygen atoms in 8, 6, and 12% of frames, respectively, all of which result in the N127 orientation away from solvent, in agreement with H/D exchange experiments (Figure 10C). R195 also stabilized a buried orientation of N127 with a side chain−side chain hydrogen bond in a total of 8% of frames (Figure 10C). In 14% of frames, the side chain nitrogen atom of N127 also formed a stable interaction with the side chain oxygen atom of N205 (Figure 10A). In this orientation, N127 also interacted with the hydroxyl side chain of S199 (in 8% of frames, Figure 10B), but interactions with S196 were not observed.

In the three representative simulation snapshots extracted (Figure 10), the average combined ϕ/ψ deviations from TALOS+ predictions were 13 ± 2, 14 ± 1, and 12 ± 1°, respectively. The RMSD of Cα atoms in loop C to 1FQY hAQP1[10] structure was (5.5, 5.5, and 5.4 Å) for each of the three snapshots, respectively, after alignment on the transmembrane segments of the reference crystal structure. Similarly, the loop C RMSD was (2.8, 5.4, and 3.8 Å), (5.4, 4.5, and 4.7 Å), and (4.9, 7.7, and 4.0 Å), for the 1J4N bAQP1,[13] 1IH5 hAQP1,[11] and refined 1H6I hAQP1[14] structures, respectively. Although these structures have a low average TALOS+ deviation, high RMSD values suggest that the selected loop C conformations deviate significantly from the existing crystal structures. Each of the three structures satisfies hydrogen bonding and solvent accessibility characteristics determined experimentally. As such, these models represent some of the best candidate structures for loop C at near physiological conditions.

DOI: 10.1021/acs.jpcb.6b06731
J. Phys. Chem. B XXXX, XXX, XXX−XXX

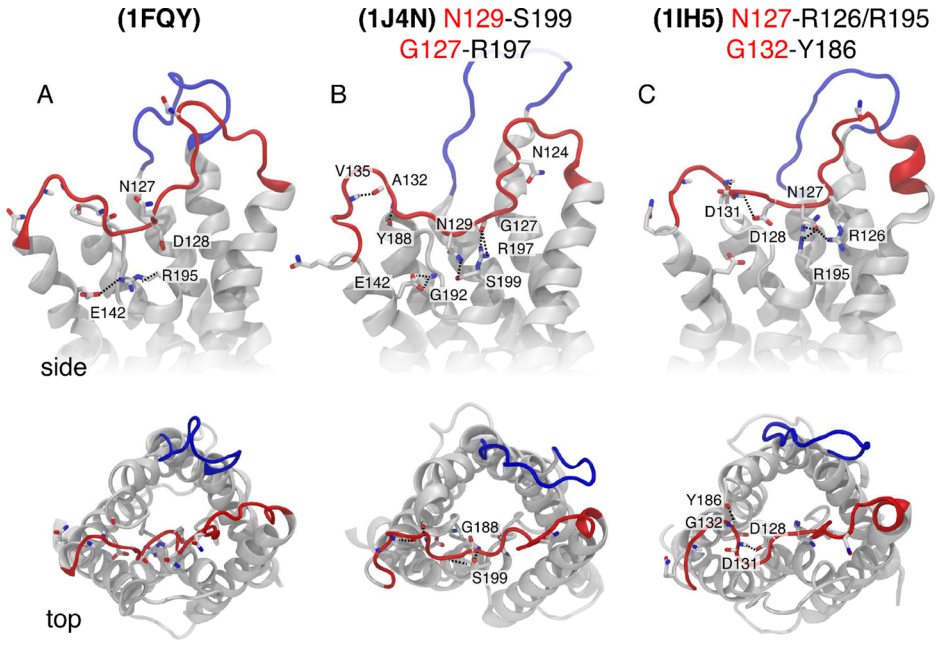

Figure 11. Multiple crystal structures of AQP1, highlighting loops A (blue) and C (red) along with key hydrogen bonds. The extracellular region of hAQP1 is shown from side and top orientations, where the side view omits residues 196−215 for clarity. A dashed line (black) indicates the presence of a hydrogen bond. (A) hAQP1 structure 1FQY,[10] exhibiting no loop C stabilizing interactions. (B) bAQP1 structure 1J4N (bovine residue numbering),[13] exhibiting a loop C beta turn, N129 interactions with S199, and R197 interactions with G127. (C) hAQP1 structure 1IH5,[11] exhibiting N127 interactions with R195.

DISCUSSION

Our experimental SSNMR results suggest that loops A and C are at least partially ordered and immobilized. Reduction or lack of signal intensity at residues 40−43 in the middle of loop A (Figure 4) suggests an increased mobility of these residues on the submicrosecond time scale. In agreement with human and bovine AQP1 structures,[10−13] restrained MD simulations reveal no stabilizing interactions for these residues, and suggest that they adopt no consensus secondary structure across models, with only a small number of frames in some of the MD models exhibiting a transient hydrogen-bonded turn or a single α-helical turn (Figure 8A). Restrained simulations indicate broad solvent accessibility across most of the loop A backbone. Thus, both experiments and simulations are consistent with a partially ordered turn facing the solvent. Here, "partially ordered" refers to the existence of some well-defined stabilizing elements in loop A, not characteristic of a fully disordered loop.

Chemical shifts indicate a Y37−P38 *cis* bond, and further suggest that β-structure may be formed in the stretches of loop A at both K36−P38 and T44−D48, flanking the flexible region. In agreement with the experimental measurements, no interactions were observed in the simulations to support a stable β-hairpin with a high population (Figure 8A). We did observe, however, a small subpopulation of β-sheet formed between neighboring subunits involving residues A45−Q47 and V46−Q47 (Figure 8B, II).

Torsional restraints derived from TALOS+ were applied to multiple residues in loop A, including the *cis* Y37−P38 bond, for XTAL and medoid A−E models. Since we did not perform restrained simulations in which the XTAL model was permitted to adopt an unrestrained *trans* Y37−P38 bond, we cannot quantify the effect of this conformer on loop A dynamics in restrained simulations. However, in control simulations performed without torsional restraints, the aromatic ring of Y37 frequently made closer stabilizing contacts with the pyrrolidine ring of P38 in each of our medoid A−E models (*cis* Y37−P38 bond) than in the XTAL model (*trans* Y37−P38 bond). We expect that the *cis* bond stabilizes the conformation of loop A and has an influence on the side chain conformations of nearby residues (K36 to V39), many of which were involved in interactions with loop C. For example, the D128−K36 salt-bridge predicted by restrained MD simulations in *cis* Y37−P38 models is consistent with the chemical shift-based prediction of the D128 side chain being strongly hydrogen bonded, and can potentially contribute to the stability of both loops A and C (Figure 10A).

TALOS+ angles for loop C indicate that β-structure exists for residues L129−N134 and restrained MD simulation results further support these conclusions. Simulations predict with high confidence (70−90% of frames) the formation of a A130−V133 β-turn with G132 adopting a (ϕ, ψ) conformation close to (80°, 0°), indicative of an ideal type II β-turn on the edge of loop C. Hydrogen bonding between A130 and V133 protects the latter from H/D exchange and is consistent with the observation of a nonexchangeable V133 amide group. Furthermore, in agreement with backbone amide burial of residues 130 and 134 in H/D exchange experiments (Figure 6A), restrained simulations suggest that this β-turn is further stabilized by a N134 backbone hydrogen bond with the side chain oxygen atom of Q137, as well as potential backbone−backbone interactions of A130 and Y186 (Figures 9B and 10A). The former interaction is not observed in any known AQP1 structure, although the A130−Y186 interaction is found in the 4CSK hAQP1 structure.[12]

The rigidity of loop C predicted by NMR experiments is likely facilitated by specific interactions at the extracellular side of hAQP1. H/D exchange experiments revealed that the side chain nitrogen of N127 and one out of three side chain nitrogen atoms of R195 were solvent inaccessible, suggesting

DOI: 10.1021/acs.jpcb.6b06731
J. Phys. Chem. B XXXX, XXX, XXX−XXX

that these residues may be involved in such interactions. Several orientations of N127 are suggested by previous structures of hAQP1, some of which result in direct interactions with R195. In the 1IH5 EM hAQP1 structure, N127 was hydrogen bonded to both R126 and R195 (Figure 11C).[11] In the 4CSK hAQP1 X-ray structure, N127 adopted a buried conformation in which it was hydrogen-bonded to both R195 and S196.[12] In the refined EM hAQP1 structure (1H6I), the N127 side chain only forms interactions with the backbone of T187.[14] Although the loop C sequence at residues 126−128 varies considerably from "RND" to "LNA" between human and bovine AQP1, the N127 side chain adopts a similar buried conformation but involves S196 in the 1J4N bAQP1 X-ray structure (Figure 11B).[13] The interaction found in the 1J4N structure was qualitatively similar to a structural model obtained from our restrained simulations wherein N127 was hydrogen bonded to both S199 and N205 (although R195 was shifted toward the backbone carbonyl groups of T187−C189 and S196 was not involved, Figure 10B). In addition, we identified several other possible solvent shielded orientations of N127, including one in which the R195 side chain is hydrogen-bonded to the backbone of nearby residues T187, G188, and C189 (Figure 10C). Our simulations suggest that N127 has a high probability of interacting with the aforementioned residues, most likely with the S199 and R195 side chains.

The exchangeability of only one of the terminal nitrogen atoms of R195 is puzzling, considering their similar (different by only ∼1 ppm) chemical shifts, as it is believed that strong asymmetry in hydrogen bonding should result in large differences in chemical shift values between the two atoms.[64] In the 1FQY EM structure of hAQP1, used as a template for MD simulations, R195 adopts a unique orientation in which it is interacting with E142, N192, S196, and C189 (Figure 11A).[10] This orientation may support the asymmetric hydrogen bonding of terminal nitrogen atoms suggested by our experiments, as hydrogen bonding of one of the R195 atoms to E142 is much weaker than that of the other to N192 (heavy atom distances are 3.39 vs 2.36 Å). Nevertheless, as this orientation of R195 faces away from the water pore and is not observed in any other AQP1 structure, it is less likely to represent a highly populated physiological conformation.

In the bAQP1 X-ray structure (1J4N), the two terminal nitrogen atoms of R195 are hydrogen bonded to the G125 backbone carbonyl (human numbering), but the hydrogen bonding distance and angles involving these atoms differ significantly (heavy atom distances are 2.93 vs 3.18 Å), suggesting that they do not interact equally (Figure 11B).[13] Even though the more distant nitrogen may also be protected by an interaction with the R195 backbone, this hydrogen bond is also weak (donor−acceptor distance of 3.17 Å), suggesting that this structure may satisfy the predicted asymmetric burial of this side chain in the physiological state of R195. Similarly, the two terminal nitrogen atoms of R195 are hydrogen bonded with the G125 backbone carbonyl and the S199 side chain in the 1H6I hAQP1 structure (heavy atom distances are 2.77 vs 2.72 Å), although this conformation does not suggest asymmetric burial of R195 terminal nitrogen atoms.[14] In the 4CSK structure of hAQP1 which used the bovine structure for model building and structure refinement, R195 is oriented such that its N_ε hydrogen bonds with C189 and the two terminal nitrogen atoms form hydrogen bonds with the backbone carbonyl of R195, the N127 side chain, and the G188 backbone.[12] Although R195 appears to be well coordinated in this structure, the closest interactions involving the terminal nitrogen atoms and the N127 side chain oxygen are strongly asymmetric (with heavy atom distances of 2.82 vs 3.12 Å). However, it is difficult to assess the actual asymmetry of terminal nitrogen burial, since both appear to be accessible by extracellular water. Lastly, in the 1IH5 structure of hAQP1, the two terminal nitrogen atoms of R195 are hydrogen bonded with the N127 side chain, and again, one of them is further protected by an interaction with the R195 backbone (Figure 11C).[11] This structure is also qualitatively consistent with asymmetric nitrogen burial, since one of the terminal nitrogen groups has a longer hydrogen bond (with donor−acceptor distances of 2.53 and 2.96 Å) and is largely oriented toward the water conduction pore, much like the bovine AQP1 structure. Thus, it is still difficult to assess if the conformation of R195 in any of the known structures is in complete agreement with the NMR data. We also note that crystallographic B-factors for side chain nitrogen atoms of R195 may result in mean-square displacements of 0.5−1.0 Å, preventing high accuracy characterization of hydrogen bonding involving the R195 guanidinium group in these structures.

One of the structures selected from restrained simulations supports asymmetric bonding of R195, with one terminal nitrogen atom coordinated to the backbone carbonyl group of T187 and the other terminal nitrogen atom facing the pore (Figure 10B). Similarly, in an alternate structure selected from restrained simulations, R195 forms a hydrogen bond with N127 via one nitrogen, and all other side chain nitrogens are solvent-exposed (Figure 10C). In MD studies of both hAQP1 and bacterial aquaporin Z, the guanidinium group of R195 adopted a side-facing orientation in which it interacted with the deprotonated N_ε of H180.[22,65] However, both the chemical shifts and H/D exchange measurements of nitrogen groups in H180 suggest that this N_ε atom is most likely protonated and thus this interaction is unlikely to result in the asymmetric burial of R195. The N_ε of H180 was protonated in our simulations, and as such, we did not observe frequent H180-facing conformations of R195.

Introducing TALOS+ derived restraints on loops A and C led to a statistically significant increase in water permeability in simulations based on the 1FQY crystal structure model (Figure 7). Although further analysis is required in order to identify the structural rearrangements responsible for this increase, this result suggests that loop conformation plays a functional role in the regulation of water. The computed water permeabilities of the different models, which fall in the range $(0.1-3) \times 10^{-14}$ cm^3/s, are commensurate with measurements (in the range 4−12)[43,66−68] and with estimates computed in previous simulation studies (in the range 0.5−10).[22,69−71]

Overall, the simulations reveal a number of loop stabilizing interactions that alter the extracellular surface of human AQP1, with possible implications for the regulation of water permeation through the channel. Previously, several mutagenesis and molecular dynamics studies of hAQP1 showed that the electrostatic and hydrogen-bonding profile of the extracellular channel entrance, in particular the ar/R selectivity filter, affect the rate and water selectivity (e.g., impermeability to cations).[15,22,72−74] Our results show that several side chains from loop C (such as N127 and D128) occupy the extracellular vestibule of hAQP1, which could modulate water permeation near the ar/R selectivity filter. This may happen as a result of direct interaction of these side chains with R195, resulting in repositioning of its positive charge in the selectivity filter, and/

DOI: 10.1021/acs.jpcb.6b06731
J. Phys. Chem. B XXXX, XXX, XXX−XXX

or by more subtle mechanisms, in which changed pattern of hydrogen bonding with other polar side chains of the extracellular vestibule (from H1, HE, and loop E) results in the rearrangement of water molecules in the channel.

Although NMR experiments suggest that loop A is partially ordered and that loop C has limited mobility, a significant portion of our simulation data set was not in direct agreement with this finding. Even in the presence of torsional restraints, it is likely that we have not yet equilibrated loop A and loop C ensembles, and that the application of even weak torsional restraints may significantly hinder conformational sampling. A previous comparison of H/D exchange data to MD simulations suggests that a hydrogen-bond-centric view of nitrogen group protection may be insufficient.[75] A more detailed discussion of sources of error in MD simulations is given in the Supporting Information.

CONCLUSION

Solid-state NMR experiments suggest that extracellular loops A and C of hAQP1 are partially ordered and possess some structural elements that were not observed in any crystallographic structure of hAQP1. Extensive conformational sampling of these loops was performed using restrained molecular dynamics simulations in order to assist in the interpretation of NMR results. Structures in agreement with experimental data suggest that loop C is stabilized by several hydrogen bonds in the extracellular vestibule of hAQP1, with possible stabilization by side chains in loop A. This work provides a detailed understanding of the hAQP1 structure in a physiologically relevant environment (lipid-reconstituted protein at near physiological temperatures) required for ongoing research examining the regulation of water conduction and the extracellular vestibule as a selective site for small molecule inhibitors of hAQP1.

ASSOCIATED CONTENT

Supporting Information

The Supporting Information is available free of charge on the ACS Publications website at DOI: 10.1021/acs.jpcb.6b06731.

Experimental details of protein synthesis and sample preparation, SAXS spectrum of the hAQP1 SSNMR sample, an example of a backbone walk for residues G125−D131, representative $^{15}N/^{13}C$ planes of the 3D NCACX experiment collected in H_2O and D_2O buffers, comparison of secondary structure elements in AQP1 across models, torsional restraint strength used in simulations, RMSD from the crystal structure and TALOS+ values over time, for all models, Ramachandran plots and average φ/ψ angle analysis for loop A and loop C residues from MD simulations, molecular renderings of multiple frames from RMSD-based clustering of loop C, percentage of restrained data set where nitrogen atoms of each residue were hydrogen bonded to protein or water oxygen atoms for all loop C clusters, and conformational states of R195 in unrestrained and restrained simulations (PDF)

AUTHOR INFORMATION

Corresponding Authors

*E-mail: lebrown@uoguelph.ca. Phone: 519-824-4120, ext. 53777.

*E-mail: vladizha@uoguelph.ca. Phone: 519-824-4120, ext. 53989.

Present Address

[#]S.W.: Beijing Nuclear Magnetic Resonance Center and College of Chemistry and Molecular Engineering, Peking University, Beijing, China 100871.

Author Contributions

[¶]S.W., C.I., and S.E. were equal contributors. S.E. prepared samples; V.L., S.W., and S.E. collected SSNMR data; S.W. and S.E. processed and analyzed SSNMR data; Y.J. and H.L. collected and analyzed SAXS data; L.S.B., R.P., and V.L. designed the study; C.I. and R.P. generated and analyzed MD data; C.I., H.L., R.P., L.S.B., and V.L. wrote the paper. All authors discussed the results of the study.

Notes

The authors declare no competing financial interest.

ACKNOWLEDGMENTS

This research was supported by NSERC Discovery Grants RGPIN-2014-04547 to V.L., RGPIN-2013-250202 to L.S.B., NSF-DMR #1623241 and NSF-CBET #1623240 to H.L., and CIHR grant MOP-130461 to R.P. Computations were performed on the GPC supercomputer at the SciNet HPC Consortium. SciNet is funded by the Canada Foundation for Innovation under the auspices of Compute Canada, the Government of Ontario, Ontario Research Fund - Research Excellence, and the University of Toronto. SAXS experiments were performed at the Stanford Synchrotron Radiation Lightsource, a national user facility operated by Stanford University on behalf of the U.S. Department of Energy, Office of Basic Energy Sciences, under Contract No. DE-AC02-76SF00515. S.W. was a recipient of the CIHR postdoctoral fellowship. S.E. was a recipient of the Ontario Trillium Scholarship.

ABBREVIATIONS

2D, two-dimensional; 3D, three-dimensional; AQP, aquaporin; bAQP1, bovine aquaporin 1; hAQP1, human aquaporin 1; ar/R, aromatic arginine constriction; BMRB, Biological Magnetic Resonance Bank; DARR, dipolar-assisted rotational resonance; EM, electron microscopy; MAS, magic angle spinning; MD, molecular dynamics; PC, phosphatidylcholine; POPC, 1-palmitoyl-2-oleoyl-*sn*-glycero-3-phosphocholine; PS, phosphatidylserine; RMSD, root-mean-square deviation; SAXS, small-angle X-ray scattering; SSNMR, solid-state NMR spectroscopy; TALOS, Torsion Angle Likeliness Obtained from Shift and Sequence Similarity

REFERENCES

(1) Stroud, R. M.; Savage, D.; Miercke, L. J. W.; Lee, J. K.; Khademi, S.; Harries, W. Selectivity and Conductance Among the Glycerol and Water Conducting Aquaporin Family of Channels. *FEBS Lett.* **2003**, *555*, 79−84.

(2) Rojek, A.; Praetorius, J.; Frøkiaer, J.; Nielsen, S.; Fenton, R. A. A Current View of the Mammalian Aquaglyceroporins. *Annu. Rev. Physiol.* **2008**, *70*, 301−327.

(3) Verkman, A. S. Aquaporins at a Glance. *J. Cell Sci.* **2011**, *124*, 2107−2112.

(4) Papadopoulos, M. C.; Verkman, A. S. Aquaporin Water Channels in the Nervous System. *Nat. Rev. Neurosci.* **2013**, *14*, 265−277.

(5) Seeliger, D.; Zapater, C.; Krenc, D.; Haddoub, R.; Flitsch, S.; Beitz, E.; Cerdà, J.; de Groot, B. L. Discovery of Novel Human Aquaporin-1 Blockers. *ACS Chem. Biol.* **2013**, *8*, 249−256.

DOI: 10.1021/acs.jpcb.6b06731
J. Phys. Chem. B XXXX, XXX, XXX−XXX

(6) Yool, A. J.; Brown, E. A.; Flynn, G. A. Roles for Novel Pharmacological Blockers of Aquaporins in the Treatment of Brain Oedema and Cancer. *Clin. Exp. Pharmacol. Physiol.* **2010**, *37*, 403−409.
(7) Haddoub, R.; Rützler, M.; Robin, A.; Flitsch, S. L. Design, Synthesis and Assaying of Potential Aquaporin Inhibitors. In *Aquaporins*; Beitz, E., Ed.; Springer: Berlin, Heidelberg, 2009; Vol. *190*, pp 385−402.
(8) Yamaguchi, T.; Iwata, Y.; Miura, S.; Kawada, K. Reinvestigation of Drugs and Chemicals as Aquaporin-1 Inhibitors Using Pressure-Induced Hemolysis in Human Erythrocytes. *Biol. Pharm. Bull.* **2012**, *35*, 2088−2091.
(9) Mola, M. G.; Nicchia, G. P.; Svelto, M.; Spray, D. C.; Frigeri, A. Automated Cell-Based Assay for Screening of Aquaporin Inhibitors. *Anal. Chem.* **2009**, *81*, 8219−8229.
(10) Murata, K.; Mitsuoka, K.; Hirai, T.; Walz, T.; Agre, P.; Heymann, J. B.; Engel, A.; Fujiyoshi, Y. Structural Determinants of Water Permeation Through Aquaporin-1. *Nature* **2000**, *407*, 599−605.
(11) Ren, G.; Reddy, V. S.; Cheng, A. Visualization of a Water-Selective Pore by Electron Crystallography in Vitreous Ice. *Proc. Natl. Acad. Sci. U. S. A.* **2001**, *98*, 1398−1403.
(12) Ruiz Carrillo, D.; To Yiu Ying, J.; Darwis, D.; Soon, C. H.; Cornvik, T.; Torres, J.; Lescar, J. Crystallization and Preliminary Crystallographic Analysis of Human Aquaporin 1 at a Resolution of 3.28 Å. *Acta Crystallogr., Sect. F: Struct. Biol. Commun.* **2014**, *70*, 1657−1663.
(13) Sui, H.; Han, B.-G.; Lee, J. K.; Walian, P.; Jap, B. K. Structural Basis of Water-Specific Transport Through the AQP1 Water Channel. *Nature* **2001**, *414*, 872−878.
(14) de Groot, B. L.; Engel, A.; Grubmüller, H. A Refined Structure of Human Aquaporin-1. *FEBS Lett.* **2001**, *504*, 206−211.
(15) Wu, B.; Steinbronn, C.; Alsterfjord, M.; Zeuthen, T.; Beitz, E. Concerted Action of Two Cation Filters in the Aquaporin Water Channel. *EMBO J.* **2009**, *28*, 2188−2194.
(16) de Groot, B. L.; Frigato, T.; Helms, V.; Grubmüller, H. The Mechanism of Proton Exclusion in the Aquaporin-1 Water Channel. *J. Mol. Biol.* **2003**, *333*, 279−293.
(17) Chakrabarti, N.; Tajkhorshid, E.; Roux, B.; Pomes, R. Molecular Basis of Proton Blockage in Aquaporins. *Structure* **2004**, *12*, 65−74.
(18) Preston, G. M.; Jung, J. S.; Guggino, W. B.; Agre, P. Membrane Topology of Aquaporin CHIP. Analysis of Functional Epitope-Scanning Mutants by Vectorial Proteolysis. *J. Biol. Chem.* **1994**, *269*, 1668−1673.
(19) Scheuring, S.; Tittmann, P.; Stahlberg, H.; Ringler, P.; Borgnia, M.; Agre, P.; Gross, H.; Engel, A. The Aquaporin Sidedness Revisited. *J. Mol. Biol.* **2000**, *299*, 1271−1278.
(20) Heymann, J. B.; Engel, A. Structural Clues in the Sequences of the Aquaporins. *J. Mol. Biol.* **2000**, *295*, 1039−1053.
(21) Buck, T. M.; Wagner, J.; Grund, S.; Skach, W. R. A Novel Tripartite Motif Involved in Aquaporin Topogenesis, Monomer Folding and Tetramerization. *Nat. Struct. Mol. Biol.* **2007**, *14*, 762−769.
(22) Hub, J. S.; Aponte-Santamaría, C.; Grubmüller, H.; de Groot, B. L. Voltage-Regulated Water Flux Through Aquaporin Channels in Silico. *Biophys. J.* **2010**, *99*, L97−L99.
(23) Yu, J.; Yool, A. J.; Schulten, K.; Tajkhorshid, E. Mechanism of Gating and Ion Conductivity of a Possible Tetrameric Pore in Aquaporin-1. *Structure* **2006**, *14*, 1411−1423.
(24) Müller, E. M.; Hub, J. S.; Grubmüller, H.; de Groot, B. L. Is TEA an Inhibitor for Human Aquaporin-1? *Pfluegers Arch.* **2008**, *456* (4), 663−669.
(25) Opella, S. J. Structure Determination of Membrane Proteins by Nuclear Magnetic Resonance Spectroscopy. *Annu. Rev. Anal. Chem.* **2013**, *6*, 305−328.
(26) Wang, S.; Ladizhansky, V. Recent Advances in Magic Angle Spinning Solid State NMR of Membrane Proteins. *Prog. Nucl. Magn. Reson. Spectrosc.* **2014**, *82*, 1−26.
(27) Baker, L. A.; Baldus, M. Characterization of Membrane Protein Function by Solid-State NMR Spectroscopy. *Curr. Opin. Struct. Biol.* **2014**, *27*, 48−55.
(28) Nyblom, M.; Öberg, F.; Lindkvist-Petersson, K.; Hallgren, K.; Findlay, H.; Wikström, J.; Karlsson, A.; Hansson, Ö.; Booth, P. J.; Bill, R. M.; et al. Exceptional Overproduction of a Functional Human Membrane Protein. *Protein Expression Purif.* **2007**, *56*, 110−120.
(29) Emami, S.; Fan, Y.; Munro, R.; Ladizhansky, V.; Brown, L. S. Yeast-Expressed Human Membrane Protein Aquaporin-1 Yields Excellent Resolution of Solid-State MAS NMR Spectra. *J. Biomol. NMR* **2013**, *55*, 147−155.
(30) Fan, Y.; Emami, S.; Munro, R.; Ladizhansky, V.; Brown, L. S. Isotope Labeling of Eukaryotic Membrane Proteins in Yeast for Solid-State NMR. In *Isotope Labeling of Biomolecules - Labeling Methods*; Kelman, Z., Ed.; Methods in Enzymology; Elsevier: Cambridge, MA, 2015; Vol. *565*, pp 193−212.
(31) Shi, L.; Ladizhansky, V. Magic Angle Spinning Solid-State NMR Experiments for Structural Characterization of Proteins. In *Intrinsically Disordered Protein Analysis: Vol. 1, Methods and Experimental Tools*; Uversky, N. V., Dunker, K. A., Eds.; Intrinsically Disordered Protein Analysis: Vol. 1, Methods and Experimental Tools; Humana Press: Totowa, NJ, 2012; pp 153−165.
(32) Baldus, M.; Petkova, A. T.; Herzfeld, J.; Griffin, R. G. Cross Polarization in the Tilted Frame: Assignment and Spectral Simplification in Heteronuclear Spin Systems. *Mol. Phys.* **1998**, *95*, 1197−1207.
(33) Takegoshi, K.; Nakamura, S.; Terao, T. 13C−1H Dipolar-Assisted Rotational Resonance in Magic-Angle Spinning NMR. *Chem. Phys. Lett.* **2001**, *344*, 631−637.
(34) Morcombe, C. R.; Zilm, K. W. Chemical Shift Referencing in MAS Solid State NMR. *J. Magn. Reson.* **2003**, *162*, 479−486.
(35) Fung, B. M.; Khitrin, A. K.; Ermolaev, K. An Improved Broadband Decoupling Sequence for Liquid Crystals and Solids. *J. Magn. Reson.* **2000**, *142*, 97−101.
(36) Fiser, A.; Šali, A. Modeller: Generation and Refinement of Homology-Based Protein Structure Models. *Methods Enzymol.* **2003**, *374*, 461−491.
(37) Wolf, M. G.; Hoefling, M.; Aponte-Santamaría, C.; Grubmüller, H.; Groenhof, G. G_Membed: Efficient Insertion of a Membrane Protein Into an Equilibrated Lipid Bilayer with Minimal Perturbation. *J. Comput. Chem.* **2010**, *31*, 2169−2174.
(38) MacKerell, A. D.; Bashford, D.; Bellott, M.; Dunbrack, R. L.; Evanseck, J. D.; Field, M. J.; Fischer, S.; Gao, J.; Guo, H.; Ha, S. A. All-Atom Empirical Potential for Molecular Modeling and Dynamics Studies of Proteins. *J. Phys. Chem. B* **1998**, *102*, 3586−3616.
(39) Best, R. B.; Zhu, X.; Shim, J.; Lopes, P. E.; Mittal, J.; Feig, M.; MacKerell, A. D., Jr. Optimization of the Additive CHARMM All-Atom Protein Force Field Targeting Improved Sampling of the Backbone Φ, ψ and Side-Chain X1 and X2 Dihedral Angles. *J. Chem. Theory Comput.* **2012**, *8*, 3257−3273.
(40) Klauda, J. B.; Venable, R. M.; Freites, J. A. Update of the CHARMM All-Atom Additive Force Field for Lipids: Validation on Six Lipid Types. *J. Phys. Chem. B* **2010**, *114*, 7830−7843.
(41) Jorgensen, W.; Chandrasekhar, J.; Madura, J. D.; Impey, R. W.; Klein, M. Comparison of Simple Potential Functions for Simulating Liquid Water. *J. Chem. Phys.* **1983**, *79*, 926−935.
(42) Pronk, S.; Pall, S.; Schulz, R.; Larsson, P.; Bjelkmar, P.; Apostolov, R.; Shirts, M. R.; Smith, J. C.; Kasson, P. M.; van der Spoel, D.; et al. GROMACS 4.5: a High-Throughput and Highly Parallel Open Source Molecular Simulation Toolkit. *Bioinformatics* **2013**, *29*, 845−854.
(43) Walz, T.; Smith, B. L.; Zeidel, M. L.; Engel, A.; Agre, P. Biologically Active Two-Dimensional Crystals of Aquaporin CHIP. *J. Biol. Chem.* **1994**, *269*, 1583−1586.
(44) Patterson, A. L. The Scherrer Formula for X-Ray Particle Size Determination. *Phys. Rev.* **1939**, *56*, 978−982.
(45) Li, Y.; Berthold, D. A.; Gennis, R. B.; Rienstra, C. M. Chemical Shift Assignment of the Transmembrane Helices of DsbB, a 20-kDa

DOI: 10.1021/acs.jpcb.6b06731
J. Phys. Chem. B XXXX, XXX, XXX−XXX

Integral Membrane Enzyme, by 3D Magic-Angle Spinning NMR Spectroscopy. *Protein Sci.* **2008**, *17*, 199−204.
(46) Shi, L.; Lake, E. M. R.; Ahmed, M. A. M.; Brown, L. S.; Ladizhansky, V. Solid-State NMR Study of Proteorhodopsin in the Lipid Environment: Secondary Structure and Dynamics. *Biochim. Biophys. Acta, Biomembr.* **2009**, *1788*, 2563−2574.
(47) Shi, L.; Kawamura, I.; Jung, K.-H.; Brown, L. S.; Ladizhansky, V. Conformation of a Seven-Helical Transmembrane Photosensor in the Lipid Environment. *Angew. Chem., Int. Ed.* **2011**, *50*, 1302−1305.
(48) Shen, Y.; Bax, A. Prediction of Xaa-Pro Peptide Bond Conformation From Sequence and Chemical Shifts. *J. Biomol. NMR* **2010**, *46*, 199−204.
(49) Schubert, M.; Labudde, D.; Oschkinat, H.; Schmieder, P. A Software Tool for the Prediction of Xaa-Pro Peptide Bond Conformations in Proteins Based on 13C Chemical Shift Statistics. *J. Biomol. NMR* **2002**, *24*, 149−154.
(50) Wu, W.-J.; Raleigh, D. P. Local Control of Peptide Conformation: Stabilization of Cis Proline Peptide Bonds by Aromatic Proline Interactions. *Biopolymers* **1998**, *45*, 381−394.
(51) Wishart, D. S.; Sykes, B. D.; Richards, F. M. The Chemical Shift Index: a Fast and Simple Method for the Assignment of Protein Secondary Structure Through NMR Spectroscopy. *Biochemistry* **1992**, *31*, 1647−1651.
(52) Kabsch, W.; Sander, C. Dictionary of Protein Secondary Structure: Pattern Recognition of Hydrogen-Bonded and Geometrical Features. *Biopolymers* **1983**, *22*, 2577−2637.
(53) Pahlke, D.; Leitner, D.; Wiedemann, U.; Labudde, D. COPS−Cis/Trans Peptide Bond Conformation Prediction of Amino Acids on the Basis of Secondary Structure Information. *Bioinformatics* **2005**, *21*, 685−686.
(54) Shen, Y.; Delaglio, F.; Cornilescu, G.; Bax, A. TALOS+: a Hybrid Method for Predicting Protein Backbone Torsion Angles From NMR Chemical Shifts. *J. Biomol. NMR* **2009**, *44*, 213−223.
(55) Lewis, P. N.; Momany, F. A.; Scheraga, H. A. Chain Reversals in Proteins. *Biochim. Biophys. Acta, Protein Struct.* **1973**, *303*, 211−229.
(56) Cotten, M.; Fu, R.; Cross, T. A. Solid-State NMR and Hydrogen-Deuterium Exchange in a Bilayer-Solubilized Peptide: Structural and Mechanistic Implications. *Biophys. J.* **1999**, *76*, 1179−1189.
(57) Wang, S.; Shi, L.; Kawamura, I.; Brown, L. S.; Ladizhansky, V. Site-Specific Solid-State NMR Detection of Hydrogen-Deuterium Exchange Reveals Conformational Changes in a 7-Helical Transmembrane Protein. *Biophys. J.* **2011**, *101*, L23−L25.
(58) Metz, G.; Siebert, F.; Engelhard, M. High-Resolution Solid State Carbon-13 NMR of Bacteriorhodopsin: Characterization of [4−13C]Asp Resonances. *Biochemistry* **1992**, *31*, 455−462.
(59) Jaroniec, C. P.; Tounge, B. A.; Herzfeld, J.; Griffin, R. G. Frequency Selective Heteronuclear Dipolar Recoupling in Rotating Solids: Accurate 13C− 15N Distance Measurements in Uniformly 13C, 15N-Labeled Peptides. *J. Am. Chem. Soc.* **2001**, *123*, 3507−3519.
(60) Fujiyoshi, Y.; Mitsuoka, K.; de Groot, B. L.; Philippsen, A.; Grubmüller, H.; Agre, P.; Engel, A. Structure and Function of Water Channels. *Curr. Opin. Struct. Biol.* **2002**, *12*, 509−515.
(61) Grossfield, A.; Feller, S. E.; Pitman, M. C. Convergence of Molecular Dynamics Simulations of Membrane Proteins. *Proteins: Struct., Funct., Genet.* **2007**, *67*, 31−40.
(62) Zhu, F.; Tajkhorshid, E.; Schulten, K. Collective Diffusion Model for Water Permeation Through Microscopic Channels. *Phys. Rev. Lett.* **2004**, *93*, 224501.
(63) Stansfeld, P. J.; Jefferys, E. E.; Sansom, M. S. P. Multiscale Simulations Reveal Conserved Patterns of Lipid Interactions with Aquaporins. *Structure* **2013**, *21*, 810−819.
(64) Petkova, A. T.; Hu, J. G.; Bizounok, M.; Simpson, M.; Griffin, R. G.; Herzfeld, J. Arginine Activity in the Proton-Motive Photocycle of Bacteriorhodopsin: Solid-State NMR Studies of the Wild-Type and D85N Proteins. *Biochemistry* **1999**, *38*, 1562−1572.
(65) Wang, Y.; Schulten, K.; Tajkhorshid, E. What Makes an Aquaporin a Glycerol Channel? a Comparative Study of AqpZ and GlpF. *Structure* **2005**, *13*, 1107−1118.
(66) Zeidel, M. L.; Ambudkar, S. V.; Smith, B. L.; Agre, P. Reconstitution of Functional Water Channels in Liposomes Containing Purified Red Cell CHIP28 Protein. *Biochemistry* **1992**, *31*, 7436−7440.
(67) Zeidel, M. L.; Nielsen, S.; Smith, B. L.; Ambudkar, S. V.; Maunsbach, A. B.; Agre, P. Ultrastructure, Pharmacologic Inhibition, and Transport Selectivity of Aquaporin CHIP in Proteoliposomes. *Biochemistry* **1994**, *33*, 1606−1615.
(68) Yang, B.; Verkman, A. S. Water and Glycerol Permeabilities of Aquaporins 1−5 and MIP Determined Quantitatively by Expression of Epitope-Tagged Constructs in Xenopus Oocytes. *J. Biol. Chem.* **1997**, *272*, 16140−16146.
(69) Hashido, M.; Ikeguchi, M.; Kidera, A. Comparative Simulations of Aquaporin Family: AQP1, AQPZ, AQP0 and GlpF. *FEBS Lett.* **2005**, *579*, 5549−5552.
(70) Zhu, F.; Tajkhorshid, E.; Schulten, K. Theory and Simulation of Water Permeation in Aquaporin-1. *Biophys. J.* **2004**, *86*, 50−57.
(71) Hashido, M.; Kidera, A.; Ikeguchi, M. Water Transport in Aquaporins: Osmotic Permeability Matrix Analysis of Molecular Dynamics Simulations. *Biophys. J.* **2007**, *93*, 373−385.
(72) Beitz, E.; Wu, B.; Holm, L. M.; Schultz, J. E.; Zeuthen, T. Point Mutations in the Aromatic/Arginine Region in Aquaporin 1 Allow Passage of Urea, Glycerol, Ammonia, and Protons. *Proc. Natl. Acad. Sci. U. S. A.* **2006**, *103*, 269−274.
(73) Hub, J. S.; Grubmüller, H.; de Groot, B. L. Dynamics and Energetics of Permeation Through Aquaporins. What Do We Learn From Molecular Dynamics Simulations? *Handb. Exp. Pharmacol.* **2009**, *190*, 57−76.
(74) Chen, H.; Wu, Y.; Voth, G. A. Origins of Proton Transport Behavior From Selectivity Domain Mutations of the Aquaporin-1 Channel. *Biophys. J.* **2006**, *90*, L73−L75.
(75) McAllister, R. G.; Konermann, L. Challenges in the Interpretation of Protein H/D Exchange Data: a Molecular Dynamics Simulation Perspective. *Biochemistry* **2015**, *54*, 2683−2692.

DOI: 10.1021/acs.jpcb.6b06731
J. Phys. Chem. B XXXX, XXX, XXX−XXX